

A Finite-Deformation Constitutive Model of Particle-Binder Composites Incorporating Yield-Surface-Free Plasticity

Ankit Agarwal

School of Mechanical Engineering,
Purdue University,
West Lafayette, IN 47907
e-mail: agarwa80@purdue.edu

Marcial Gonzalez¹

School of Mechanical Engineering;
Ray W. Herrick Laboratories,
Purdue University,
West Lafayette, IN 47907
e-mail: marcial-gonzalez@purdue.edu

We present a constitutive model for particle-binder composites that accounts for finite-deformation kinematics, nonlinear elastoplasticity without apparent yield, cyclic hysteresis, and progressive stress-softening before the attainment of stable cyclic response. The model is based on deformation mechanisms experimentally observed during quasi-static monotonic and cyclic compression of mock plastic-bonded explosives (PBX) at large strain. An additive decomposition of strain energy into elastic and inelastic parts is assumed, where the elastic response is modeled using Ogden hyperelasticity while the inelastic response is described using yield-surface-free endochronic plasticity based on the concepts of internal variables and of evolution or rate equations. Stress-softening is modeled using two approaches; a discontinuous isotropic damage model to appropriately describe the softening in the overall loading–unloading response, and a material scale function to describe the progressive cyclic softening until cyclic stabilization. A nonlinear multivariate optimization procedure is developed to estimate the elastoplastic model parameters from nominal stress–strain experimental compression data. Finally, a correlation between model parameters and the unique stress–strain response of mock PBX specimens with differing concentrations of aluminum is identified, thus establishing a relationship between model parameters and material composition. [DOI: 10.1115/1.4052654]

Keywords: constitutive modeling of materials, mechanical properties of materials, endochronic plasticity

1 Introduction

Particle-binder composite materials consist of a large concentration of hard particles, called fillers, randomly dispersed in the matrix of a soft material. Generally, fillers are used to enhance the mechanical properties of the soft material. For example, filled elastomers such as carbon-black and silica filled rubbers [1,2] have been shown to possess superior stiffness, strength, and damping properties over natural rubber, making them suitable for application in automotive parts such as tires and bearing seals and in structures providing vibration and shock isolation to mechanical systems.

Another class of particle-binder composites, called energetic composite materials or plastic-bonded explosives (PBX), consists of explosive crystals and, in some formulations, metal fuel powder, embedded in a binder composed mainly of a soft polymer and a plasticizer. Since their initial development at Los Alamos National Laboratory in 1947, PBXs have been commonly used as ammunition in defense applications. Examples of explosives used include cyclotrimethylenetrinitramine (RDX) and cyclotetra-minetetranitramine (HMX), while the binder composition includes polymers like hydroxyl-terminated polybutadiene (HTPB) and Estane, and plasticizers like dioctyl adipate (DOA) and isodecyl pelargonate (IDP), along with smaller concentrations of various additives [3]. In a PBX binder, the polymer, apart from providing structural integrity to the explosive, reduces their impact and vibrational sensitivity [4–6], while the plasticizer

improves their mechanical properties and processability [7]. The metal fuel, usually aluminum, is used to enhance the blast effects. Therefore, aluminized PBXs are typically used in naval weapons and missile warheads [8].

Energetic composites are commonly used in applications requiring high mechanical confinement or compression [9,10]. Additionally, these materials may be subjected to diverse loading conditions, ranging from low to high strain-rate cyclic, vibrational and impact loading during transport, storage and handling over their operational life. Since PBXs are designed to detonate under specific external energy stimulus, such loading conditions may alter their mechanical response, rendering them unpredictable and unsafe [11]. Therefore, understanding and predicting the mechanical response of PBX under different loading conditions is of particular interest to the defense and propulsion communities.

Earlier experimental studies on the mechanical behavior of PBX under uniaxial load have shown a dependence on strain rate and temperature [12–14]. Several constitutive models in the context of small and large deformation mechanics have been developed to model their rate and temperature-dependent behavior. For instance, Bardenhagen et al. [15] proposed a large deformation viscoelastic model for PBX binder materials using a Blatz-Ko hyperelasticity formulation and a Maxwell element. Clements and Mas [16] proposed a viscoelastic constitutive theory for filled polymers using the Boltzmann superposition principle, where the filler particles were modeled as randomly positioned elastic ellipsoidal particles. Composite stress relaxation functions were developed with their prony series coefficients dependent on filler concentration, ellipsoidal aspect ratio, and polymer moduli. The viscoelastic cracking constitutive model developed by Bennet et al. [17] combined a linear viscoelastic Maxwell's model with the isotropic damage model by Addessio and Johnson [18]. It was based on the mechanism of microcracking and derived from the statistical crack mechanics approach proposed by Dienes [19] for brittle materials. The model was developed to predict the nonlinear stress–strain response

¹Corresponding author.

Contributed by the Applied Mechanics Division of ASME for publication in the JOURNAL OF APPLIED MECHANICS. Manuscript received August 19, 2021; final manuscript received September 26, 2021; published online October 22, 2021. Assoc. Editor: Shengping Shen.

The United States Government retains, and by accepting the article for publication, the publisher acknowledges that the United States Government retains, a nonexclusive, paid-up, irrevocable, worldwide license to publish or reproduce the published form of this work, or allow others to do so, for United States government purposes.



Fig. 1 Mock PBX specimens

of the material, as well as the strain-softening and nonlinearity observed due to extensive cracking at larger deformations. The model has since been extensively implemented in finite element analyses and used to predict the thermo-mechanical behavior of PBX and study hotspot generation [6,20]. In the context of PBX undergoing low-frequency vibrational loading, nonlinear viscoelastic models for a mass-material system undergoing base excitation were proposed by Paripovic and Davies [21,22].

While the majority of constitutive formulations proposed for the PBX model the material as viscoelastic due to the rubbery nature of the polymer binder, it has been shown that these materials may exhibit considerable plastic deformation with increasing confinement. Uniaxial confined compression tests carried out on inert mock sugar-based specimens for PBX 9501 [9,10] under different confining pressures revealed increasing plastic deformation and strain hardening with increasing pressure. Recently, Agarwal and Gonzalez [23] conducted unconfined compression tests at room temperature and low strain rate (10^{-3} /s) on cylindrical specimens of three mock explosive formulations (Fig. 1) based on PBXN-109 [24], with sugar as a substitute for the explosive HMX crystals. The three formulations contained 85% w/w of solids (sugar and aluminum) but differed from each other by the amount of aluminum content in the solids composition, namely, 85-00 (0% Al in solids, 0% in total), 85-15 (15% Al in solids, 12.75% in total) and 85-30 (30% additive in solids, 25.5% in total). The monotonic nominal stress-strain response of the 85-00 specimen (Fig. 2(a)) exhibited a quasi-brittle behavior [25], with an initial nonlinear increase in stress until a peak stress level at around 10–11% strain, followed by strain-softening due to the evolution of microcracks into larger transgranular fracture leading to a loss of strength. Such behavior has been recorded and studied extensively for many non-aluminized PBX formulations [6,12,26]. However, the aluminized specimens, i.e., 85-15 (Fig. 2(b)) and 85-30 (Fig. 2(c)) exhibited a more ductile plastic flow behavior with strain hardening, indicating that the presence of aluminum could cause the material to deform plastically even in the absence of confinement.

Additionally, plastic deformation and damage in PBX have been shown to be associated with hotspot mechanisms [27,28], thus directly impacting their ignition characteristics. Therefore, the development of a constitutive model capable of characterizing the plastic behavior of explosives is extremely important for proper modeling and prediction of their mechanical behavior. Constitutive models for PBX incorporating plasticity have been proposed for cyclic deformation [29] and mild impact [30]. However, the models have been developed using small deformation theory and, therefore, are inapplicable to the large deformation mechanical behavior of explosives.

Lastly, Agarwal and Gonzalez [23] also conducted cyclic compression tests of the mock PBX specimens at room temperature and low strain rate (10^{-3} /s). Figure 3 shows the nominal cyclic stress-strain response of the specimens. The strain-controlled tests were carried out by initially loading the specimen to a maximum strain level, and thereafter partially unloading-reloading between

the maximum and a minimum strain. The optimal minimum-maximum strain levels were identified for each mock PBX composition through a systematic procedure detailed in Ref. [23] that was developed to ensure sufficiently large elastoplastic deformation while preventing the material to reach its ultimate strength as well as keep the specimen in compression throughout the loading process. Through this procedure, the cyclic strain levels were identified as 5–9% for 85-00, 8–16% for 85-15, and 6–9% for 85-30. Observable response attributes (indicated in the figures) include the following: (1) a nonlinear, continuous elastoplastic response without apparent yield, (2) hysteresis, and (3) cyclic stress-softening with eventual stabilization. It is also worth noting that the curvature of the initial loading path is different from those of subsequent reloading paths. The former is convex and the latter are concave, indicating irreversible changes in the material behavior during the initial loading itself. This behavior has also been previously observed for cyclic compression of aluminized RDX-based PBX in HTPB binder [31].

It is apparent that the observed mechanical response of mock PBX specimens exhibits similar characteristics to filled elastomers at large deformations. Constitutive models of filled elastomers have been proposed by adopting both phenomenological [32–37] and micromechanical [38–40] frameworks. For instance, Ayoub et al. [33] proposed a Zener-type visco-hyperelastic constitutive model of rubber-like materials that accounts for the Mullins effect [41,42], continuous stress-softening, and permanent residual strains by utilizing the network alteration theory [43,44]. Raghunath et al. [39] extended the micromechanical dynamic flocculation model developed by Klüppel [45] to include time-dependent effects typical of filled elastomers. It is worth mentioning that the majority of these models attribute the observed hysteresis and other inelastic phenomena to time-dependent viscous overstress in the rubber matrix. In contrast, only a limited number of models consider these phenomena as time-independent plastic deformation mechanisms. A case in point is the phenomenological elastoplastic constitutive model proposed by Kaliske and Rothert [46] that captures the rate-independent process of internal material friction due to irreversible polymer slippage on the filler surface and plastic deformation of the filler particles. This multi-yield-surface rheological model is comprised of a finite number of elastoplastic Prandtl elements arranged in parallel with an elastic member. More recently, yield-surface-free endochronic plasticity [47] was utilized by Netzker et al. [48] to model the smooth and hysteretic cyclic stress-strain response of carbon-black filled rubbers, with higher computational efficiency and fewer parameters.

In this paper, we present an elastoplastic constitutive formulation with isotropic damage capable of modeling the cyclic response of mock energetic composite materials. Specifically, a Lagrangian finite-deformation formulation based on the additive decomposition of strain energy [49–53] into elastic and plastic parts is adopted. The formulation uses Ogden's hyperelastic model [54,55] to predict the rubber-like nonlinear elastic response of the polymeric binder and a hereditary (path-dependent) yield-surface-free endochronic plasticity theory [47], based on the concept of internal state variables [56],

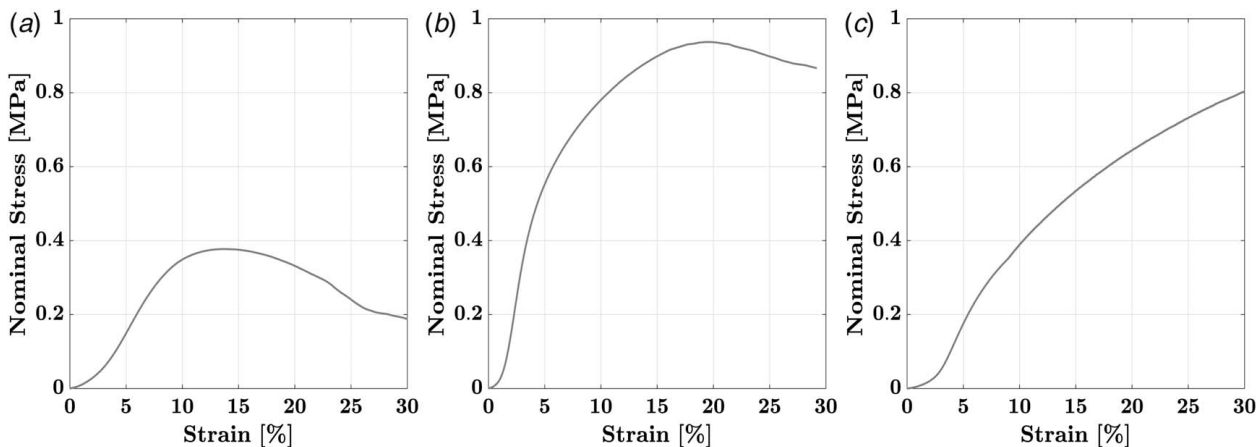


Fig. 2 (a) Uniaxial monotonic compressive stress–strain response of (a) 85–00, (b) 85–15, and (c) 85–30 mock PBX specimens recorded for a maximum applied strain of 30%

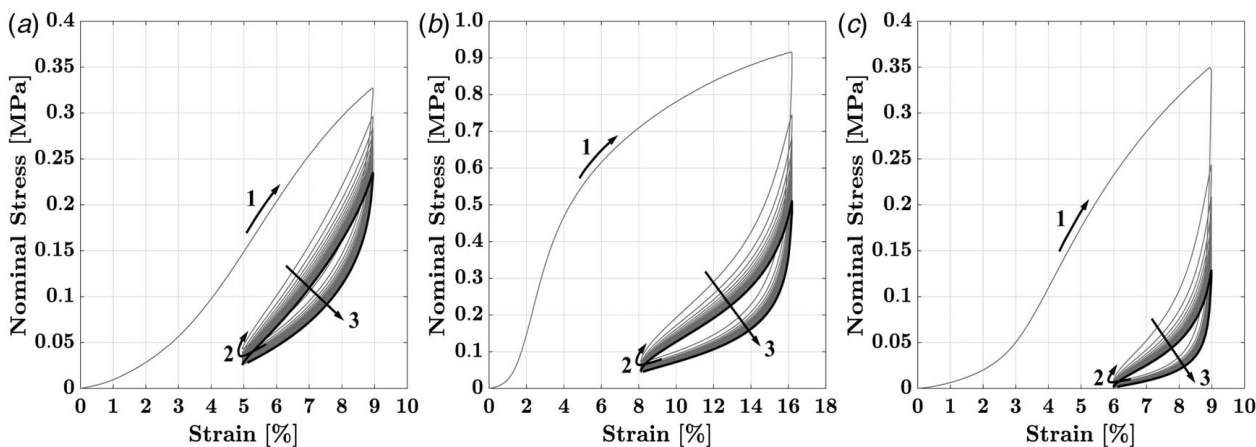


Fig. 3 (a) Nominal stress–strain response under strain-controlled unconfined uniaxial compressive cyclic loading of (a) 85–00, (b) 85–15, and (c) 85–30 mock PBX specimens. The response until the attainment of a stable cyclic loop is shown in gray, while the stable cyclic loop is shown in black. Observable response attributes (labeled in the figures) include the following: (1) highly nonlinear stress–strain response without a distinctive yield point, (2) hysteresis, and (3) cyclic stress-softening with eventual stabilization.

to account for irreversible deformations. A discontinuous isotropic damage model [57,58] is utilized to model the stress-softening that occurs during unloading, and an endochronic material scale function is utilized to model progressive cyclic stress-softening and attainment of stable cyclic response. It is worth mentioning that while the material scale function has been utilized in previous works to describe the cyclic hardening or softening behavior of metals and alloys [47,59–61], its application to filled polymeric materials with complex microstructure like particle-binder composites has not been demonstrated in the open literature, and thus, it is one of the primary contributions of this paper. The number of model parameters is a function of the number of active Ogden terms and endochronic branches; therefore, a significant number of parameters may need to be identified. Accordingly, we develop a parameter identification method based on a nonlinear multivariate least-squares problem, which is expected to be non-convex and affected by multiple local optima. The range of behavior predicted by the proposed model is demonstrated by calibrating the model parameters for the three mock PBX material compositions [23] under both monotonic and cyclic compressive loading. Finally, the versatility and the capability of the model to represent the material, specifically, the material composition, is demonstrated by identifying a correlation between the calibrated model parameters and the unique stress–strain response of each mock PBX specimen.

The paper is organized as follows. The constitutive model is presented in Sec. 2, followed by Sec. 3 which provides a discrete

numerical procedure to solve for stresses along a loading path. Section 4 presents the model parameter identification procedure and the calibrated material properties of the three mock PBX formulations. Section 5 shows a detailed comparative analysis of the three specimen formulations and presents the correlation identified between the estimated mechanical properties and the mechanical behavior, as well as the composition of the specimens. Finally, a summary and concluding remarks are presented in Sec. 6.

2 Constitutive Model

2.1 General Framework. The finite-deformation constitutive law is based on an additive decomposition of the Helmholtz free energy density function [49–53] into elastic and plastic parts, and it employs a local multiplicative decomposition of the deformation gradient into isochoric and volumetric contributions. This approach is in contrast to the constitutive formulations based on the multiplicative elastic–plastic decomposition of the deformation gradient [62–65] or additive decomposition of the rate of deformation tensor [66–68]. For an isothermal elastoplastic deformation process, the free energy density function Ψ is given by

$$\Psi(\mathbf{C}, \zeta_1, \dots, \zeta_N) = \Psi_{\text{vol}}^e(J) + \Psi_{\text{iso}}^e(\bar{\mathbf{C}}) + \sum_{j=1}^N \Gamma_j^e(\mathbf{C}, \zeta_j) \quad (1)$$

where $\Psi_{\text{vol}}^e(J)$ and $\Psi_{\text{iso}}^e(\bar{\mathbf{C}})$ are the volumetric and isochoric elastic strain energy density functions, dependent respectively, on the Jacobian of the deformation $J = \det(\mathbf{F})$ and on the isochoric right Cauchy-Green deformation tensor $\bar{\mathbf{C}} = \bar{\mathbf{F}}^T \bar{\mathbf{F}}$ (where $\bar{\mathbf{F}} = J^{-1/3} \mathbf{F}$). The inelastic strain energy $\sum_{j=1}^N \Gamma_j^i(\mathbf{C}, \zeta_j)$ is a set of configurational free energy functions Γ_j^i ($j = 1, \dots, N$) that characterizes the inelastic deformation behavior, namely, irreversible slip at particle–particle and particle–binder contacts, plastic deformation, and fracture of particles, among other dissipative mechanisms typical of particle–binder composites. This path-dependent dissipative potential depends on the right Cauchy-Green deformation tensor \mathbf{C} and a set of inelastic strain-like second-order tensorial internal variables ζ_j ($j = 1, \dots, N$) that represent the inelastic deformation history of the material.

Additionally, filled rubber or soft polymeric materials in general exhibit a stress-softening behavior when unloaded from a maximum previous deformation. This phenomenon, widely known as the Mullins effect [41,42], has been discussed extensively in the literature. The micromechanics behind the occurrence of this phenomenon is highly debated, and numerous theories have been suggested, such as rupture of filler-polymer bonds [69,70], molecular slipping on the filler surface [71,72], and breakage of filler clusters [73,74]. However, most phenomenological descriptions of this effect employ the thermodynamic framework of continuum damage mechanics (CDM) [57,58], where the loss of the material's ability to sustain load due to damage is described by applying a scalar reduction factor, also known as a damage variable, to the stress in a hypothetical, undamaged material. Various models based on this principle have been proposed, generally classified according to the evolution of damage being discontinuous [49,75–77] or continuous [78–81] (for more information on the physical interpretation and classification of phenomenological models for Mullins effect [82]). While discontinuous damage models predict the same reloading response as the unloading response during cyclic loading (referred to as idealized Mullins effect), continuous models have the capability to model diverging unloading–reloading responses. Since the different unloading–reloading responses as seen in energetic composites can be effectively modeled by the proposed path-dependent constitutive formulation, the damage evolution can be defined as discontinuous and occurring only during unloading for simplicity and computational efficiency.

Discontinuous damage models, specifically, the pseudoelastic material models [75,77,83], are based on the application of suitable damage or softening function ϕ to the strain energy in a hypothetical, undamaged material. The evolution of this damage function is discontinuous and depends on the deformation history of the material. For a given deformation measure ϕ and its maximum value $\phi^{\text{max}} = \max_{\tau \in [-\infty, t]} \phi(\tau)$ throughout the material's deformation history until the current time t , the damage function ϕ is given by

$$\phi \begin{cases} = 1, & \phi = \phi^{\text{max}} \\ \in (0, 1), & \phi < \phi^{\text{max}} \end{cases} \quad (2)$$

Therefore, during the initial loading of the virgin material when the current value of the deformation remains equal to its maximum value throughout the material's history, the damage function does not evolve, and the material's strain energy remains unchanged. However, during unloading–reloading from a previous maximum deformation, the current deformation measure is lower than the maximum value, and the damage function evolves monotonically between 0 and 1. This in turn reduces the effective strain energy in the material and produces the softening effect.

With the application of the damage function, the effective strain energy density function $\underline{\Psi}$ is given by

$$\underline{\Psi}(\mathbf{C}, \zeta_1, \dots, \zeta_N, \phi) = \phi(\phi, \phi^{\text{max}}) \Psi(\mathbf{C}, \zeta_1, \dots, \zeta_N) \quad (3)$$

To explore the thermodynamic consistency of the constitutive model by means of fulfillment of the second law of

thermodynamics, we utilize the Clausius–Duhem inequality for an isothermal process, given by

$$\mathcal{D} := \frac{1}{2} \mathbf{S} : \dot{\mathbf{C}} - \dot{\underline{\Psi}} \geq 0 \quad (4)$$

where \mathcal{D} is the dissipation and \mathbf{S} is the second Piola-Kirchhoff stress tensor. By applying the definition of effective strain energy density function $\underline{\Psi}$ according to Eqs. (3) and (1), the inequality becomes

$$\left[\mathbf{S} - 2\phi \frac{\partial \underline{\Psi}}{\partial \mathbf{C}} \right] : \frac{\dot{\mathbf{C}}}{2} - \dot{\Psi} \phi - \sum_{j=1}^N \frac{\partial \Gamma_j^i}{\partial \zeta_j} : \dot{\zeta}_j \geq 0 \quad (5)$$

From standard arguments [84,85], the first term yields the definition of the second Piola-Kirchhoff stress, that is

$$\mathbf{S} = 2\phi \frac{\partial \Psi(\mathbf{C}, \zeta_1, \dots, \zeta_N)}{\partial \mathbf{C}} = \phi \left[\mathbf{S}_{\text{vol}}^e + \mathbf{S}_{\text{iso}}^e + \sum_{j=1}^N \mathbf{S}_j^i \right] \quad (6)$$

while the second and third terms yield the dissipation

$$\mathcal{D} = -\dot{\Psi} \phi - \sum_{j=1}^N \frac{\partial \Gamma_j^i}{\partial \zeta_j} : \dot{\zeta}_j \geq 0 \quad (7)$$

where the volumetric elastic stress $\mathbf{S}_{\text{vol}}^e$, the isochoric elastic stress $\mathbf{S}_{\text{iso}}^e$, the inelastic stress $\sum_{j=1}^N \mathbf{S}_j^i$, the thermodynamic force q (conjugate to damage function ϕ), and the stress-like internal variables $\tilde{\mathbf{S}}_j^i$ (thermodynamically conjugate to ζ_j) are given by

$$\mathbf{S}_{\text{vol}}^e = J \frac{d\Psi_{\text{vol}}^e(J)}{dJ} \mathbf{C}^{-1} \quad (8)$$

$$\mathbf{S}_{\text{iso}}^e = J^{-2/3} \text{DEV} \left\{ 2 \frac{\partial \Psi_{\text{iso}}^e(\bar{\mathbf{C}})}{\partial \bar{\mathbf{C}}} \right\} \quad (9)$$

$$\sum_{j=1}^N \mathbf{S}_j^i = 2 \sum_{j=1}^N \frac{\partial \Gamma_j^i(\mathbf{C}, \zeta_j)}{\partial \mathbf{C}} \quad (10)$$

$$q = \frac{\partial \underline{\Psi}}{\partial \phi} = \Psi \quad (11)$$

$$\tilde{\mathbf{S}}_j^i = - \frac{\partial \underline{\Psi}}{\partial \zeta_j} = - \frac{\partial \Gamma_j^i(\mathbf{C}, \zeta_j)}{\partial \zeta_j} \quad (j = 1, \dots, N) \quad (12)$$

In Eq. (9), $\text{DEV}\{\cdot\} = \{\cdot\} - (1/3)[\{\cdot\} : \mathbf{C}] \mathbf{C}^{-1}$ provides the deviator of a tensor in the reference configuration. It is worth noting that the second term of the dissipation \mathcal{D} from Eq. (7) (now given by $\sum_{j=1}^N \tilde{\mathbf{S}}_j^i : \dot{\zeta}_j$ using Eq. (12)) becomes positive by defining a flow rule of the following form

$$\dot{\zeta}_j = \mathbb{B}_j(\mathbf{C}, \zeta_j) : \tilde{\mathbf{S}}_j^i \quad (13)$$

where \mathbb{B}_j is a positive definite fourth-order tensor [52].

2.2 Elastic Strain Energy. The nonlinear elastic constitutive behavior of rubber-like materials, such as the binder in the application studied here, is commonly described through hyperelastic material models (see, e.g., the finite-deformation formulations presented in Refs. [54,55,86–88]). Ogden's hyperelastic model [54,55] is one of the most extensively used models for describing complex nonlinear responses, mainly due to its flexible series representation with the capability to introduce several model parameters.

Specifically, the isochoric elastic strain energy density Ψ_{iso}^e is given by

$$\Psi_{\text{iso}}^e(\bar{\mathbf{C}}) = \sum_{k=1}^M \frac{\mu_k}{\alpha_k} (\bar{\lambda}_1^{\alpha_k} + \bar{\lambda}_2^{\alpha_k} + \bar{\lambda}_3^{\alpha_k} - 3) \quad (14)$$

where the isochoric principal stretches are given by $\bar{\lambda}_a = J^{-1/3} \lambda_a$ ($a = 1, 2, 3$) for principal stretches λ_a ($a = 1, 2, 3$). Constants μ_k and α_k ($k = 1, \dots, M$) are material parameters that satisfy the following inequality to enforce stability in the material response

$$\mu_k \alpha_k > 0 \quad \forall k \in [1, M] \quad (15)$$

From consistency conditions with respect to linear elasticity at small strain [89], the reference (ground-state) shear modulus of the material is given by

$$\mu = \sum_{k=1}^M \frac{\mu_k \alpha_k}{2} \quad (16)$$

2.3 Discontinuous Isotropic Damage. As seen in Sec. 2.1, a discontinuous isotropic damage model is utilized to model the stress-softening that occurs during unloading, i.e., the Mullins effect [41,42] for polymeric materials, with damage function $\varphi(\phi, \phi^{\text{max}})$. In the spirit of the damage function proposed by Zúñiga and Beatty [77] and pseudoelastic damage functions proposed by Ogden and Roxburgh [75] and Dorfmann and Ogden [76], we specifically define the scalar damage variable as follows:

$$\varphi(\phi, \phi^{\text{max}}) = \tanh^p \left(\frac{\phi^{\text{max}} - \phi}{m} \right) \quad (17)$$

where the deformation measure ϕ is taken as the one proposed by Beatty and coworkers [77,90], given by

$$\phi = |\mathbf{C}| = \sqrt{\mathbf{C}:\mathbf{C}} \quad (18)$$

and where ϕ^{max} is the maximum deformation level given by

$$\phi^{\text{max}}(t) = \max_{\tau \in [-\infty, t]} \phi(|\mathbf{C}(\tau)|) \quad (19)$$

The damage function is then a monotonic function of the deformation measure in the interval $\phi \in [\sqrt{3}, \phi^{\text{max}}]$, with positive damage parameters m and p .

2.4 Yield-Surface-Free Endochronic Plasticity and Evolution Equation. As explained previously, particle-binder composites, specifically plastic-bonded explosives (PBX), exhibit a nonlinear elastoplastic response without apparent yield. Classical plasticity theories require a yield surface, and thus, their applicability is limited for modeling these composites. In this study, we follow the work of Holzapfel and Simo [51] and assume a quadratic relationship between free energy functions $\Gamma_j^i(\mathbf{C}, \zeta_j)$ and the internal variables ζ_j , i.e.,

$$\frac{\partial \Gamma_j^i}{\partial \zeta_j \zeta_k} = 2\mu_j \delta_{jk} \mathbb{1} \quad (j \text{ not summed}) \quad (20)$$

where μ_j are the reference (ground-state) shear moduli related to j inelastic processes, δ_{mn} is the Kronecker delta and $\mathbb{1}$ is the fourth-order identity tensor. Therefore, by integrating Eq. (13) twice, the following inelastic strain energy functions are obtained

$$\Gamma_j^i(\mathbf{C}, \zeta_j) = \mu_j |\zeta_j|^2 + \mathbf{S}_j^*(\mathbf{C}) : \zeta_j + \Psi_j^*(\mathbf{C}) \quad (j = 1, \dots, N) \quad (21)$$

where $\mathbf{S}^*(\mathbf{C})$ and $\Psi^*(\mathbf{C})$ are unknown tensor and scalar-valued functions, respectively. Similarly, an evolution or rate equation for the stress-like internal variables is obtained from Eqs. (12), (13), and (21), and it is given by

$$\dot{\tilde{\mathbf{S}}}_j^i + 2\mu_j \mathbb{B}_j(\mathbf{C}, \zeta_j) : \dot{\tilde{\mathbf{S}}}_j^i = -\dot{\mathbf{S}}^*(\mathbf{C}) \quad (j = 1, \dots, N) \quad (22)$$

The inelastic strain energy without apparent yield is realized by adopting the endochronic plasticity theory developed by Valanis [47]. This theory is strain path-dependent in nature, and it does not require the definition of a yield surface. It has been applied successfully to develop both infinitesimal-strain and finite-deformation plastic formulations to describe many metals and alloys [59,91,92], concrete [93], powder compaction [94–96] and, more recently, filled elastomers [37,48]. In accordance with this theory, we specifically assume the fourth-order tensor \mathbb{B}_j to be given by

$$\mathbb{B}_j(\mathbf{C}, \zeta_j) = \frac{\dot{z}(|\dot{\mathbf{C}}|)}{2\mu_j \gamma_j} \quad (j = 1, \dots, N) \quad (23)$$

where the intrinsic time scale z is a monotonically increasing measure of the deformation history, and the memory kernel is given by a set of positive dimensionless material parameters γ_j ($j = 1, \dots, N$) [95,97] that defines the path-dependent behavior of the formulation. It is worth noting that $\mu_j \gamma_j \geq 0$ for \mathbb{B}_j to be a positive definite tensor. In addition, we assume

$$\begin{aligned} \mathbf{S}_j^*(\mathbf{C}) &= -\mathbf{S}_{\text{iso},j}^e(\mathbf{C}) \\ &= -J^{-2/3} \text{DEV} \left\{ 2 \frac{\partial \Psi_{\text{iso},j}^e(\bar{\mathbf{C}})}{\partial \bar{\mathbf{C}}} \right\} \quad (j = 1, \dots, N) \end{aligned} \quad (24)$$

where $\Psi_{\text{iso},j}^e$ are a set of isochoric elastic strain energy functions defined according to Ogden's model as

$$\Psi_{\text{iso},j}^e = \sum_{i=1}^P \frac{\mu_{ij}}{\alpha_{ij}} (\bar{\lambda}_1^{\alpha_{ij}} + \bar{\lambda}_2^{\alpha_{ij}} + \bar{\lambda}_3^{\alpha_{ij}} - 3) \quad (j = 1, \dots, N) \quad (25)$$

with constants μ_{ij} and α_{ij} such that $\mu_{ij} \alpha_{ij} > 0$ (Eq. (15)). It is worth noting that after substituting \mathbb{B}_j and \mathbf{S}_j^* according to Eqs. (23) and (24), respectively, the evolution or rate Eq. (22) simplifies to

$$\dot{\tilde{\mathbf{S}}}_j^i + \frac{\dot{z}(|\dot{\mathbf{C}}|)}{\gamma_j} \tilde{\mathbf{S}}_j^i = \dot{\mathbf{S}}_{\text{iso},j}^e \quad (j = 1, \dots, N) \quad (26)$$

which can be regarded as the nonlinear extension of the one-dimensional isothermal evolution equation for a standard linear solid proposed by Valanis [98] (see Sec. 6 of the reference). Furthermore, by eliminating time dependence on both sides of the differential Eq. (26) and integrating with respect to the intrinsic time scale z , the classical hereditary or convolution form is recovered, that is

$$\tilde{\mathbf{S}}_j^i = \tilde{\mathbf{S}}_{j,0}^i + \int_0^z \dot{\mathbf{S}}_{\text{iso},j}^e e^{-\frac{z-z'}{\gamma_j}} dz' \quad (j = 1, \dots, N) \quad (27)$$

with $\tilde{\mathbf{S}}_j^i(z=0) = \tilde{\mathbf{S}}_{j,0}^i$. Finally, for completeness, we set $\Psi_j^*(\mathbf{C}) = \Psi_{\text{iso},j}^e(\bar{\mathbf{C}})$ and, therefore, the reference shear moduli μ_j in Eq. (21) are given by

$$\mu_j = \sum_{i=1}^P \frac{\mu_{ij} \alpha_{ij}}{2} > 0 \quad (j = 1, \dots, N) \quad (28)$$

2.5 Intrinsic Time Scale and Material Scale Function. The intrinsic time scale z , used in the evolution or rate Eq. (26) for internal variables $\tilde{\mathbf{S}}_j^i$, is defined as

$$\dot{z}(|\dot{\mathbf{C}}|) = \frac{|\dot{\mathbf{C}}|}{f(z)} \quad (29)$$

where $f(z)$ is a material scale function that represents the transient cyclic behavior of the material until attainment of a stable response.

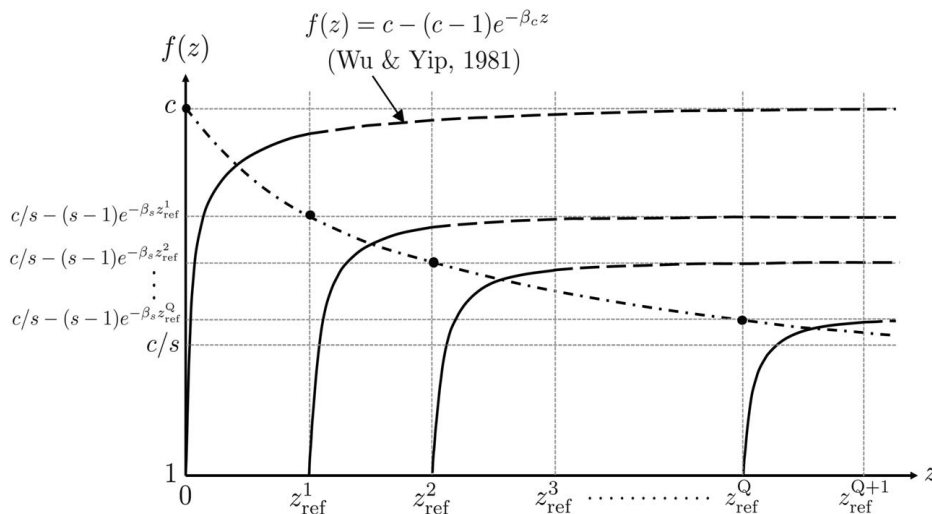


Fig. 4 Schematic representation of the evolution of material scale function $f(z)$

In its simplest form, $f(z)$ is a monotonically increasing function for cyclic hardening materials, and a monotonically decreasing function for cyclic softening materials, that is asymptotic to a saturation value at steady-state. A simple scale function proposed by Wu and Yip [59] is given by

$$f(z) = c - (c - 1)e^{-\beta_c z} \quad (30)$$

where β_c controls the rate of evolution, and the value at steady-state is $c > 1$, for hardening materials, and $c < 1$, for softening materials. Yeh [60] and Lin et al. [61] proposed the following improvements to the scale function

$$f(z) = \frac{c}{s - (s - 1)e^{-\beta_s z_{ref}}} - \left(\frac{c}{s - (s - 1)e^{-\beta_s z_{ref}}} - 1 \right) e^{-\beta_c (z - z_{ref})} \quad (31)$$

In the above improved scale function, the additional parameter z_{ref} , defined as the value of z at which the last reversal of the strain path occurred, adds the capability to model “fading memory” effects exhibited by materials with memory [99]. In turn, the saturation value at steady-state depends on the reference time scale z_{ref} . It is equal to c for $z_{ref} = 0$, i.e., before the first reversal, and approaches c/s for $z_{ref} \rightarrow \infty$, i.e., at cyclic stabilization. It is worth noting that for $c > s > 1$, the initial saturation value c is greater than the saturation value c/s at cyclic stabilization, i.e., the scale function describes the progressive cyclic softening typically observed in particle-binder composites. Figure 4 shows a schematic representation of the scale function proposed by Lin et al. [61]. It is evident from the figure that the rate of evolution of the material scale function is controlled by β_c , whereas the rate of evolution of the saturation value is controlled by β_s .

2.6 Inelastic Stress. The inelastic stress contributions \mathbf{S}_j^i ($j = 1, \dots, N$) are determined by using Eq. (10) with the inelastic strain energy function defined by Eq. (21) and by expressing the internal variables ζ_j in terms of their conjugates $\tilde{\mathbf{S}}_j^i$, i.e., using Eq. (12). The result of this mathematical manipulation is given by

$$\mathbf{S}_j^i = \mathbf{S}_{iso,j}^e - \frac{1}{\mu_j} \frac{\partial \mathbf{S}_{iso,j}^e}{\partial \mathbf{C}} : (\mathbf{S}_{iso,j}^e - \tilde{\mathbf{S}}_j^i) \quad (32)$$

where the internal variables $\tilde{\mathbf{S}}_j^i$ are determined using the evolution or rate Eq. (26).

3 Incremental Solution Procedure

The constitutive model presented in the previous section is integrated by using an incremental solution procedure with time or loading intervals $[n, n + 1]$. We assume that the state of the material, $\mathbf{C}_n, \tilde{\mathbf{S}}_{j,n}^i, z_n, z_{ref,n}, \phi_n^{\max}$, is known at loading step n and that \mathbf{C}_{n+1} at loading step $n + 1$ is given. The problem is then to determine $\tilde{\mathbf{S}}_{j,n+1}^i, z_{n+1}, z_{ref,n+1}$, and ϕ_{n+1}^{\max} at loading step $n + 1$, and the value of the second Piola-Kirchhoff stress \mathbf{S}_{n+1} , which is given by

$$\mathbf{S}_{n+1} = \varphi_{n+1} \left[\mathbf{S}_{vol,n+1}^e + \mathbf{S}_{iso,n+1}^e + \sum_{j=1}^N \mathbf{S}_{iso,j,n+1}^e - \sum_{j=1}^N \frac{1}{2\mu_j} \bar{\mathbf{C}}_{j,n+1} : (\mathbf{S}_{iso,j,n+1}^e - \tilde{\mathbf{S}}_{j,n+1}^i) \right] \quad (33)$$

where

$$\bar{\mathbf{C}}_{j,n+1} = 2 \left[\frac{\partial \mathbf{S}_{iso,j}^e}{\partial \mathbf{C}} \right]_{n+1} \quad (34)$$

and

$$\tilde{\mathbf{S}}_{j,n+1}^i = \frac{(1 - \Delta z / 2\gamma_j) \tilde{\mathbf{S}}_{j,n}^i + (\mathbf{S}_{iso,j,n+1}^e - \mathbf{S}_{iso,j,n}^e)}{(1 + \Delta z / 2\gamma_j)} \quad (35)$$

In the previous equations, all quantities other than φ_{n+1} and Δz are either known or depend on the right Cauchy-Green deformation tensor through Eqs. (8), (9), and (24). The scalar damage function φ_{n+1} is computed after updating ϕ_{n+1}^{\max} using Eq. (19). The stress-like internal variables $\tilde{\mathbf{S}}_{j,n+1}^i$ defined by Eq. (35) above are obtained by using a midpoint rule to discretize the evolution or rate Eq. (26), i.e., from

$$\tilde{\mathbf{S}}_{j,n+1}^i - \tilde{\mathbf{S}}_{j,n}^i + \left(\frac{\Delta z}{\gamma_j} \right) \left(\tilde{\mathbf{S}}_{j,n}^i + \frac{\tilde{\mathbf{S}}_{j,n+1}^i - \tilde{\mathbf{S}}_{j,n}^i}{2} \right) = \mathbf{S}_{iso,j,n+1}^e - \mathbf{S}_{iso,j,n}^e \quad (36)$$

The value of intrinsic time scale increment, Δz , is obtained by using a midpoint rule to discretize Eq. (29) together with Eq. (31), i.e., from

$$\Delta z \left[\frac{c}{s-(s-1)e^{-\beta_s z_{\text{ref},n+1}}} - \left(\frac{c}{s-(s-1)e^{-\beta_s z_{\text{ref},n}}} - 1 \right) e^{-\beta_c(z_n + \frac{\Delta z}{2} - z_{\text{ref},n+1})} \right] - |\bar{\mathbf{C}}_{n+1} - \bar{\mathbf{C}}_n| = 0 \quad (37)$$

with $z_{n+1} = z_n + \Delta z$, and

$$z_{\text{ref},n+1} = \begin{cases} z_n & \text{if } (\phi_{n+1} - \phi_n) \cdot (\phi_n - \phi_{n-1}) < 0 \\ z_{\text{ref},n} & \text{otherwise} \end{cases} \quad (38)$$

The previous nonlinear equation is solved numerically using a Newton-Raphson method.

4 Model Parameter Identification of Mock Plastic-Bonded Explosives

The range of behavior predicted by the proposed constitutive model is demonstrated by calibrating the model parameters for the three mock PBX formulations (85–00, 85–15, and 85–30) under monotonic and cyclic compression [23]. Therefore, Sec. 4.1 presents the incremental procedure for uniaxial loading under unconfined lateral conditions and incompressible material assumptions. Section 4.2 presents a parameter identification procedure based on a nonlinear multivariate minimization problem and the least-squares principle. Finally, Sec. 4.3 shows the results of the parameter identification.

4.1 Incremental Procedure for Uniaxial Cyclic Loading.

The material is assumed to be incompressible, i.e., $J_n = 1$, and thus $\bar{\mathbf{C}}_n = \mathbf{C}_n$, due to the rubber-like behavior of the particle-binder composite. The cylindrical mock PBX specimen is loaded along its axial direction which is coincidental with the \mathbf{e}_3 of a Cartesian coordinate system \mathbf{e}_l , with $l = 1, 2, 3$. Therefore, the right Cauchy–Green deformation tensor has principal stretches λ_l are related by

$$\lambda_{1,n} = \lambda_{2,n} = \frac{1}{\sqrt{\lambda_{3,n}}} \quad (39)$$

and principal directions aligned with the Cartesian axes, i.e.,

$\mathbf{C}_n = \sum_{l=1}^3 \lambda_{l,n}^2 \mathbf{e}_l \otimes \mathbf{e}_l$. The specimen is laterally unconfined and the platens that apply the load are frictionless. Therefore, the only component of the second Piola–Kirchhoff stress that is different from zero is $S_{33,n}$.

The elastic strain energy functions involved in the formulation reduce to

$$\Psi^e(\lambda_1, \lambda_2, \lambda_3) = \sum_{k=1}^M \frac{\mu_k}{\alpha_k} (\lambda_1^{\alpha_k} + \lambda_2^{\alpha_k} + \lambda_3^{\alpha_k} - 3)$$

$$\Psi_j^e(\lambda_1, \lambda_2, \lambda_3) = \sum_{i=1}^P \frac{\mu_{ij}}{\alpha_{ij}} (\lambda_1^{\alpha_{ij}} + \lambda_2^{\alpha_{ij}} + \lambda_3^{\alpha_{ij}} - 3) \quad (40)$$

$(j = 1, \dots, N)$

$$\Psi_{\text{vol}}^e(J) = -p_o(J - 1)$$

where the last term is used to augment the energy density and enforce the material internal or kinematic constraint imposed by incompressibility, i.e., $J = 1$, with p_o being the hydrostatic pressure.

Following the incremental procedure presented in Sec. 3, we assume that the state of the material, \mathbf{C}_n , $\tilde{\mathbf{S}}_{j,n}^i$, z_n , $z_{\text{ref},n}$, and ϕ_n^{max} , is known at loading step n , and that \mathbf{C}_{n+1} at loading step $n + 1$ is given. The maximum deformation level ϕ_{n+1}^{max} is determined from Eqs. (18) and (19) using

$$\phi_{n+1} = \sqrt{\lambda_{3,n+1}^4 + \frac{2}{\lambda_{3,n+1}^2}} \quad (41)$$

The intrinsic time scale increment Δz is obtained using Eq. (37) with

$$|\bar{\mathbf{C}}_{n+1} - \bar{\mathbf{C}}_n| = \sqrt{2(\lambda_{3,n+1}^{-1} - \lambda_{3,n}^{-1})^2 + (\lambda_{3,n+1}^2 - \lambda_{3,n}^2)^2} \quad (42)$$

and $z_{\text{ref},n+1}$ is updated using Eq. (38) and $z_{n+1} = z_n + \Delta z$. The stress components in Eq. (33) simplify to

$$S_{11,\text{iso},n+1}^e = S_{22,\text{iso},n+1}^e = \sum_{k=1}^M \mu_k \lambda_{3,n+1}^{1-\alpha_k/2}$$

$$S_{11,\text{vol},n+1}^e = S_{22,\text{vol},n+1}^e = -p_{o,n+1} \lambda_{3,n+1}$$

$$S_{11,\text{iso},j,n+1}^e = S_{22,\text{iso},j,n+1}^e = \sum_{i=1}^P \mu_{ij} \lambda_{3,n+1}^{1-\alpha_{ij}/2}$$

$$\bar{\mathbf{C}}_{1111,j,n+1} = \bar{\mathbf{C}}_{2222,j,n+1} = \sum_{i=1}^P \mu_{ij} (\alpha_{ij} - 2) \lambda_{3,n+1}^{2-\alpha_{ij}/2} \quad (43)$$

$$S_{33,\text{iso},n+1}^e = \sum_{k=1}^M \mu_k \lambda_{3,n+1}^{\alpha_k-2}$$

$$S_{33,\text{vol},n+1}^e = -p_{o,n+1} \lambda_{3,n+1}^{-2}$$

$$S_{33,\text{iso},j,n+1}^e = \sum_{i=1}^P \mu_{ij} \lambda_{3,n+1}^{\alpha_{ij}-2}$$

$$\bar{\mathbf{C}}_{3333,j,n+1} = \sum_{i=1}^P \mu_{ij} (\alpha_{ij} - 2) \lambda_{3,n+1}^{\alpha_{ij}-4}$$

where the hydrostatic pressure $p_{o,n+1}$ is obtained from the traction free boundary condition, i.e., from $S_{11,n+1} = S_{22,n+1} = 0$, and it is given by

$$p_{o,n+1} = \frac{1}{\lambda_{3,n+1}} \left[S_{11,\text{iso},n+1}^e + \sum_{j=1}^N S_{11,\text{iso},j,n+1}^e - \sum_{j=1}^N \frac{1}{2\mu_j} \bar{\mathbf{C}}_{1111,j,n+1} : (S_{11,\text{iso},j,n+1}^e - \tilde{\mathbf{S}}_{11,j,n+1}^i) \right] \quad (44)$$

and the stress-like internal variables $\tilde{\mathbf{S}}_{j,n+1}^i$ are readily computed using Eq. (35).

4.2 Parameter Identification Method. We have developed a parameter identification method based on a nonlinear multivariate minimization problem. The proposed constitutive model has $2M + 2P \times N + N + 6$ material parameters, namely

- (1) $2M$ parameters in the elastic branch: μ_k and α_k ($k = 1, \dots, M$).
- (2) $2P \times N$ elastic parameters in the yield-surface-free endochronic branches: μ_{ij} and α_{ij} ($i = 1, \dots, P; j = 1, \dots, N$).
- (3) N kernel parameters in the yield-surface-free endochronic branches: γ_j ($j = 1, \dots, N$).
- (4) Four material scale function parameters: c , s , β_c , and β_s .
- (5) Two isotropic damage parameters: m and p .

The method is based on the least-squares principle, for experimental monotonic and cyclic nominal stress values T_k^{exp} ($k = 1, \dots, \mathcal{K}$) and T_l^{exp} ($l = 1, \dots, \mathcal{L}$), respectively, and corresponding model first Piola–Kirchhoff stress values $\lambda_{3,k} S_{33,k}$

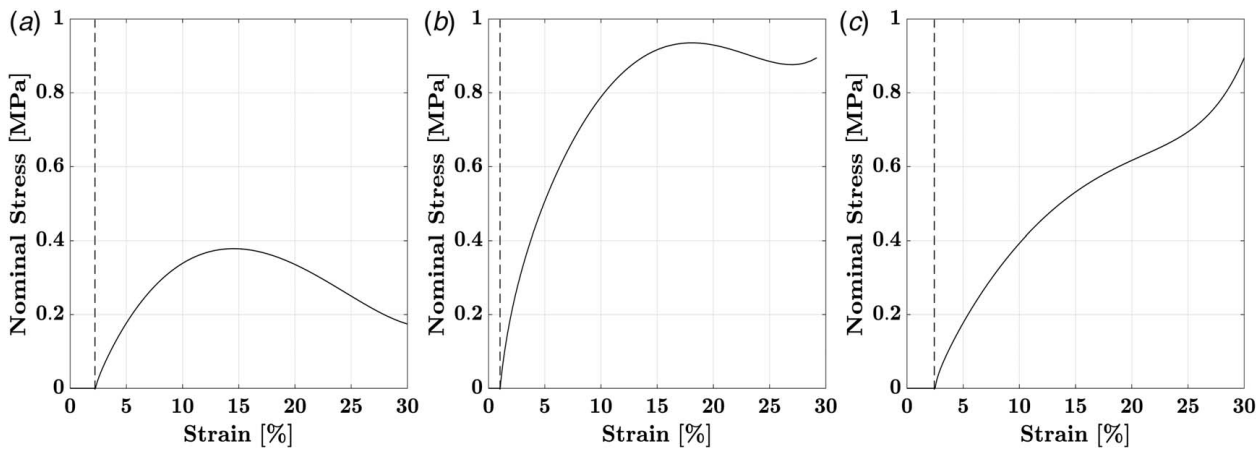


Fig. 5 (a) Model-estimated uniaxial monotonic compressive stress–strain response of (a) 85–00, (b) 85–15, and (c) 85–30 mock PBX specimens. The dashed line indicates the applied strain offset ϵ_o .

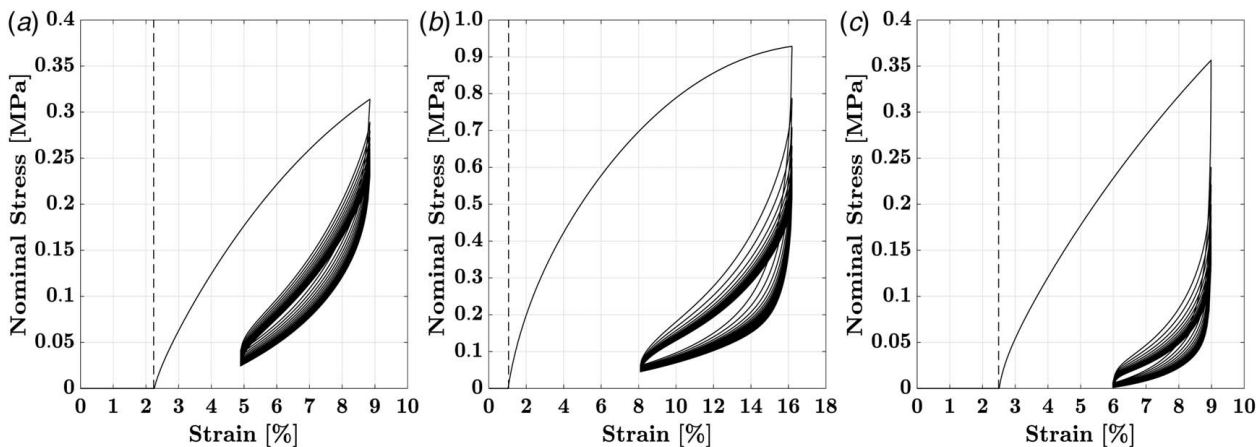


Fig. 6 (a) Model-estimated stress–strain response under strain-controlled unconfined uniaxial compressive cyclic loading of (a) 85–00, (b) 85–15, and (c) 85–30 mock PBX specimens. The dashed line indicates the applied strain offset ϵ_o .

and $\lambda_{3,l}S_{33,l}$. It is given by

$$\begin{aligned} \min_{\mathbf{v} \in \mathbb{R}^{2M+2P+N+6, \epsilon_o}} & \frac{1}{\mathcal{K}} \left[w^{\text{mono}} \sum_{k=1}^{\mathcal{K}} (T_k^{\text{exp}} - \lambda_{3,k}S_{33,k})^2 \right] \\ & + \frac{1}{\mathcal{L}} \left[w^{\text{cyclic}} \sum_{l=1}^{\mathcal{L}} (T_l^{\text{exp}} - \lambda_{3,l}S_{33,l})^2 \right] \\ \text{subject to } & -\mu_k \alpha_k \leq 0 \text{ for } k = 1, \dots, M \\ & -\mu_{ij} \alpha_{ij} \leq 0 \text{ for } i = 1, \dots, P; j = 1, \dots, N \\ & s - c \leq 0 \\ & \mathbf{v} \in [\mathbf{v}^{\min}, \mathbf{v}^{\max}] \end{aligned} \quad (45)$$

where w^{mono} and w^{cyclic} are appropriate weights applied to the monotonic and cyclic least-squares functions, respectively, to balance the accuracy of model predictions for these tests. The inequality constraints come from Ogden’s stability conditions (e.g., from Eq. (19) for the elastic branch) and from the requirement of progressive cyclic softening. Since the nonlinear optimization problem is expected to be non-convex and affected by multiple local optima, appropriate bounds are applied to the set of material parameters \mathbf{v} . Lastly, the experimental stress–strain response of the mock PBX specimens suggests that the initial loading response is affected by machine/specimen mismatch (Figs. 2 and 3). Therefore, the initial part of the response is omitted from the parameter

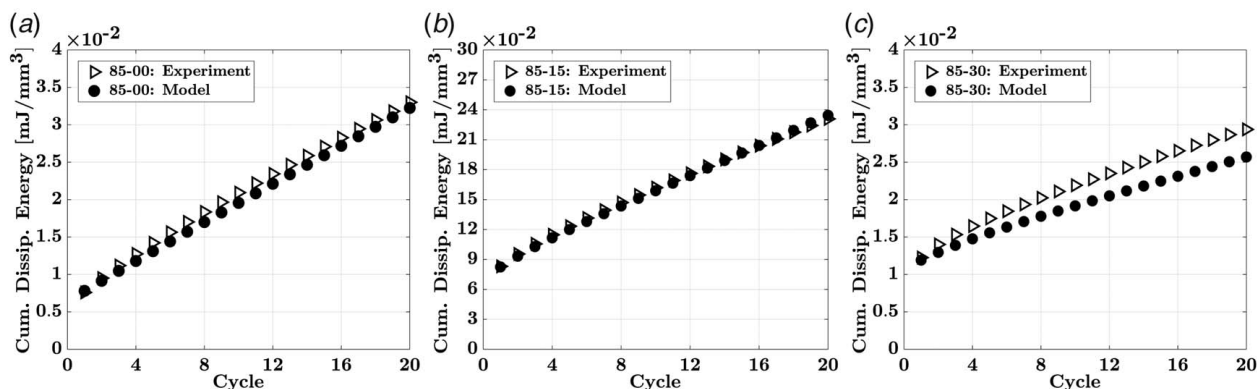
estimation by applying a strain offset ϵ_o to the experimental data and setting stresses for the initial mismatch to be zero.

An iterative procedure is followed to determine the number of terms M and P in the Ogden strain energy series functions for the elastic branch and the endochronic branches, respectively, as well as to determine the number of endochronic branches N . The procedure starts from an initial value of $M = P = N = 1$ and calculates the least-squares error given by Eq. (45). During each iteration, three error values are computed by independently incrementing the values of M , P , and N by 1. The increment corresponding to the minimum of the three errors is adopted, only if the minimum error is reduced by a specified percentage tolerance (taken as 5% in this study) as compared to the minimum error computed in the previous iteration. Otherwise, the values of M , P , and N obtained during the previous iteration are adopted and the procedure is concluded. This procedure aims to improve the estimation of the model without overly increasing its complexity.

4.3 Parameter Identification of Mock Plastic-Bonded Explosives. The constitutive model and parameter identification method presented earlier were used to calibrate the experimental monotonic (Fig. 2) and cyclic (Fig. 3) compressive response of 85–00, 85–15, and 85–30 mock PBX cylindrical specimens. The nonlinear multivariate minimization problem was solved in MATLAB® [100] using the constrained optimization function *fmincon* with the default interior-point algorithm. The model-calibrated nominal stress–strain curves are presented in Figs. 5

Table 1 Model parameters of 85–00, 85–15, and 85–30 mock energetic formulations estimated from their monotonic and cyclic compressive response

Material parameters	85–00	85–15	85–30
Elastic branch ($M=1$)			
μ_1 (MPa)	1.1252	0.7483	0.0808
α_1	9.2293	10.8969	17.4232
Initial shear modulus $\mu^e = \sum_{k=1}^M \mu_k \alpha_k / 2$ (MPa)	5.1922	4.0768	0.7037
Yield-surface-free endochronic branch 1 ($P=1$)			
μ_{11} (MPa)	0.0432	5.6465	12.1770
α_{11}	0.0519	0.8418	1.1832
Initial shear modulus $\mu_1^i = \sum_{i=1}^P \mu_{i1} \alpha_{i1} / 2$ (MPa)	0.0011	2.3766	7.2038
γ_1	0.0017	0.0010	0.0018
Yield-surface-free endochronic branch 2 ($P=1$)			
μ_{12} (MPa)	0.0068	2.8725	0.0039
α_{12}	0.0661	1.5255	0.0543
Initial shear modulus $\mu_2^i = \sum_{i=1}^P \mu_{i2} \alpha_{i2} / 2$ (MPa)	0.0002	2.1910	0.0001
γ_2	0.1723	0.0358	0.0622
Yield-surface-free endochronic branch 3 ($P=1$)			
μ_{13} (MPa)	–	4.3973	0.6204
α_{13}	–	1.6687	1.2223
Initial shear modulus $\mu_3^i = \sum_{i=1}^P \mu_{i3} \alpha_{i3} / 2$ (MPa)	–	3.6688	0.3792
γ_3	–	0.3413	0.2388
Material scale function			
c	14.9879	29.5182	591.1894
s	1.2592	2.0384	5.9671
β_c	125.3399	944.2924	2.0906
β_s	212.6798	16.7109	5.7283
Isotropic damage			
m	0.0247	0.0863	0.0195
p	0.7619	0.5769	0.3208

**Fig. 7** (a) Comparison of experimental and model-estimated cumulative energy dissipation versus number of cycles for cyclic compressive stress–strain response of (a) 85–00, (b) 85–15, and (c) 85–30 mock PBX specimens

(monotonic) and 6 (cyclic), and the estimated material parameters for each specimen formulation are listed in Table 1. Comparison of experimental and model curves suggests an excellent agreement between the two for all three formulations. The strain offset was calculated as 2.25% for 85–00, 1.03% for 85–15, and 2.51% for 85–30, and it is denoted in the figures by a dashed line.

For detailed comparative analysis, experimental and model-estimated values of the cumulative energy dissipation (Fig. 7), peak stress (Fig. 8), and apparent modulus (Fig. 9) are compared for cyclic compression of the specimens. The apparent modulus [23,37] is calculated as the slope of the line connecting peak and valley stresses in each cycle, while the cyclic energy dissipation [23] is calculated as the difference between the energy supplied to the material (i.e., the area under the loading path) and the energy recovered after a cycle (i.e., the area under the unloading path). Again, an excellent agreement between the experimental and model values is obtained for the three specimens, demonstrating the capability of the proposed model to describe the strength, stiffness, and softening characteristics of particle-binder composites.

5 Comparative Analysis of Mock Plastic-Bonded Explosives Formulations and the Relationship Between Model Parameters and Material Composition

From the observation of calibrated properties of mock PBX specimens in Table 1, it is possible to identify the correlation between the property values and the unique mechanical behavior of each specimen and, therefore, establish the relationship between material properties and material composition. For instance, the 85–00 specimen is accurately modeled by two endochronic branches, while 85–15 and 85–30 specimens require three endochronic branches to fully represent their mechanical response, which signifies the higher material nonlinearity and more extensive inelastic behavior of the aluminized specimens. Specific trends in individual property values are also observed, which are discussed in detail below.

5.1 Elastic and Endochronic Branches. In the context of representing the deformation mechanics of particle-binder

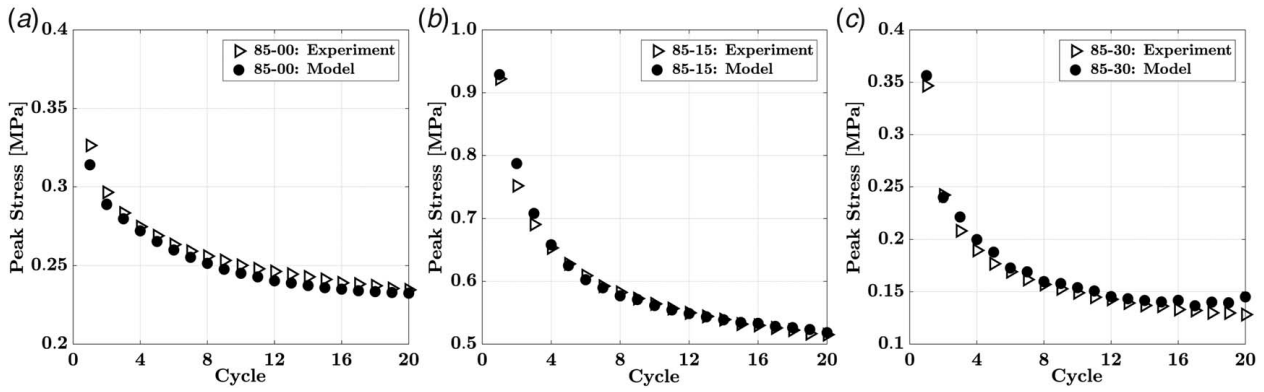


Fig. 8 (a) Comparison of experimental and model-estimated peak stress versus number of cycles for cyclic compressive stress-strain response of (a) 85-00, (b) 85-15, and (c) 85-30 mock PBX specimens

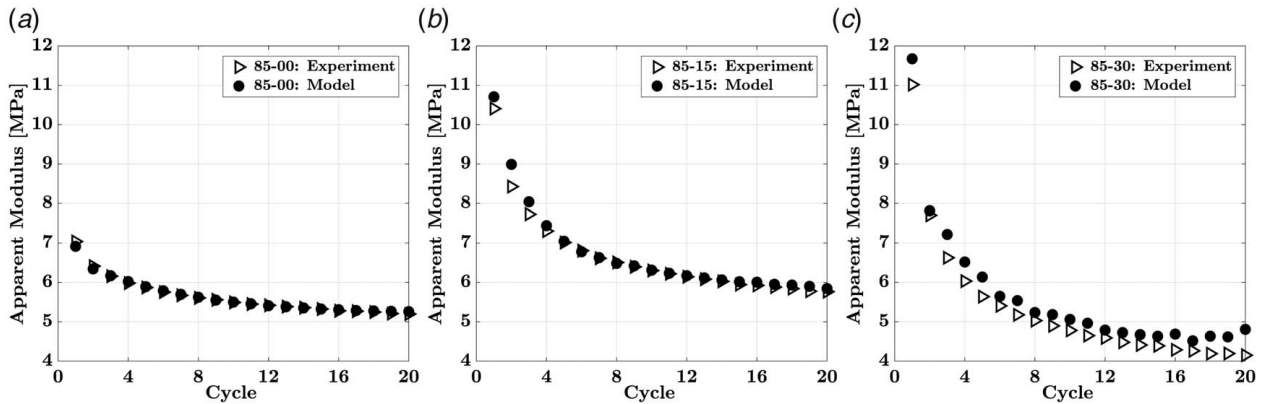


Fig. 9 (a) Comparison of experimental and model-estimated apparent modulus versus number of cycles for cyclic compressive stress-strain response of (a) 85-00, (b) 85-15, and (c) 85-30 mock PBX specimens

composites by a linear rheological model (Fig. 10) with respect to the constitutive formulation presented in Sec. 2, the elastic branch can be seen as a spring of stiffness $2\mu^e$ acting in parallel with N endochronic branches, each of which consists of a spring of stiffness $2\mu_j^i$ and a friction element with threshold strain γ_j , where $j = 1, \dots, N$. The total stiffness μ of the material is represented by a sum of the elastic and endochronic moduli, i.e., $\mu = \mu^e + \sum_{j=1}^N \mu_j^i$, while the threshold strains represent the macroscopic strains at the activation of inelastic processes, such as irreversible slipping of

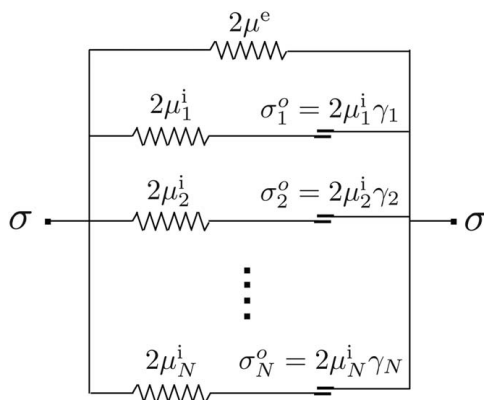


Fig. 10 Linear rheological interpretation of the proposed constitutive model

binder molecular chains on the filler (solid) surface and plastic deformation of the solid particles [46,48].

From the calibrated parameter values listed in Table 1, the total stiffness of 85-00, 85-15, and 85-30 specimens is found to be 5.1941 MPa, 12.3132 MPa, and 8.2868 MPa, respectively. This suggests that the addition of aluminum in the PBX composition increases material stiffness; however, the stiffness starts to reduce with an increase in the amount of aluminum in the composition. This postulation is also supported by the evolution of the apparent modulus during the cyclic loading of the three compositions (Fig. 9). The figures show that the apparent modulus of the cyclic loops ranges between 5 MPa and 7 MPa for 85-00, 6 MPa and 11 MPa for 85-15, and 4 MPa and 11 MPa for 85-30. Therefore, the experimentally determined average modulus follows the same order with respect to the material composition as the model-estimated modulus. Another interesting observation lies in the contribution to the total modulus by the endochronic branches, which from Table 1 is 0.0013 MPa (0.025%) for 85-00, 8.2364 MPa (66.89%) for 85-15 and 7.5831 MPa (91.51%) for 85-30. Therefore, it is evident that with the activation of inelastic deformation mechanisms, the elastic material stiffness decreases with increasing aluminum content, which is also consistent with the observation of predominantly nonlinear mechanical response and ductile plastic flow to larger strain levels during monotonic compression in 85-15 and 85-30 as compared to 85-00 (Fig. 2).

With regard to the threshold strains γ_j , the value of strain γ_1 in the first endochronic branch is very small and comparable in magnitude for all PBX compositions (0.0017 for 85-00, 0.001 for 85-15, and 0.0018 for 85-30). This suggests that mock PBX material starts

exhibiting inelastic behavior from almost the beginning of the loading process regardless of aluminum content, which rationalizes the selection of a yield surface-free plasticity theory to model these materials. However, the value of threshold strain in the second endochronic branch (γ_2) is much larger for 85–00 (0.1723) as compared to those of 85–15 (0.0358) and 85–30 (0.0622), indicating that more extensive inelastic processes start occurring at smaller macroscopic strains in the aluminized specimens. When comparing 85–15 and 85–30 specimens, we observe that although the second threshold strain is smaller for 85–15, the threshold strain in the third branch (γ_3) is smaller for 85–30 (0.2388) as compared to 85–15 (0.3413). Therefore, it can be concluded that higher aluminum content leads to the material exhibiting predominant inelastic deformations at a smaller strain. This conclusion is also supported by observations of higher residual strain in 85–30 (~2%) as compared to 85–15 (~1.57%) after the recovery period following the virgin cyclic loading tests as observed by Agarwal and Gonzalez [23].

5.2 Material Scale Function. As explained in Sec. 2.5, the material scale function $f(z)$, which is a function of the intrinsic time scale z , is used in the constitutive model to represent the progressive cyclic stress-softening behavior observed during cyclic compression of particle-binder composites. The function is given by Eq. (31) and consists of four material parameters, namely, c , s , β_c , and β_s . The parameter c is the saturation value of the function during initial loading from zero deformation when the reference intrinsic time scale, z_{ref} , is equal to zero. If the loading remains monotonic, the simpler scale function proposed by Wu and Yip [59] and given by Eq. (30) is recovered. According to this simpler function, the value of $f(z)$ evolves from 1 as z increases and approaches c at $z \rightarrow \infty$, with the rate of evolution governed by β_c . If $c > 1$, then $f(z) \geq 1$. Therefore, during a loading step, the increment in the intrinsic time scale z is greater than the increment in deformation measure $|C|$ according to Eq. (29), which produces a strain-hardening behavior. Conversely, if $c < 1$, a strain-softening response is obtained. This is also true during cyclic loading–unloading; however, the saturation value changes as z_{ref} increases, and approaches c/s at $z_{\text{ref}} \rightarrow \infty$ which signifies cyclic stabilization. If $c/s < c$, then a progressive stress-softening response is obtained, which, as already stated, is one of the primary deformation mechanisms observed in mock PBX.

The value of parameter c for the studied mock PBX specimens is seen to increase with increasing aluminum content in the composition. Specifically, it is much higher for 85–30 as compared to 85–00 and 85–15 specimens. The reason for this difference lies in the monotonic compression response of the specimens. Figure 11 shows the influence of variation in c from its estimated value on

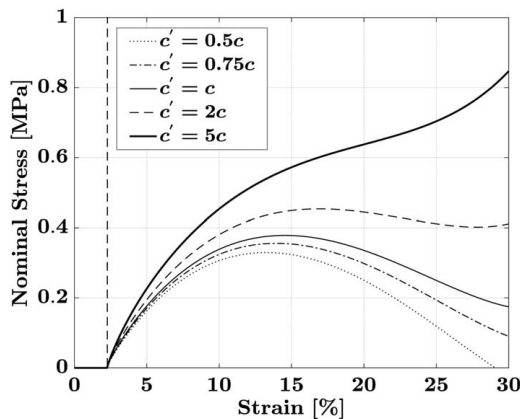


Fig. 11 Influence of variation in the value of material scale function parameter c on the predicted monotonic compressive response of 85–00 formulation

the monotonic compression response of 85–00 specimen. It is evident that c controls the occurrence of maximum or ultimate stress in the response, as well as the magnitude of the ultimate stress, which stems from its representative role as the magnitude of strain hardening in the material. The ultimate stress is observed in the monotonic response of 85–00 and 85–15 specimens, with the value of the stress and the strain at which it occurs is higher for 85–15 as compared to that for 85–00. Therefore, the estimated value of parameter c for 85–15 is comparatively higher than for 85–00. However, the 85–30 specimen does not show an ultimate stress and continues to harden until the maximum applied deformation of 30%; hence, in accordance with Fig. 11, the estimated value of c for 85–30 is much higher than both 85–00 and 85–15. With regard to parameter β_c , a correlation between the estimated values and PBX aluminum content is not observed; rather, the values are closely related to the evolution of the scale function during monotonic loading and the estimated values of c . Figure 12 shows the influence of variation in β_c on the monotonic compression response as well as the evolution of scale function $f(z)$ with intrinsic time z for the three specimens. It is evident that for 85–00 and 85–15 specimens, the scale function $f(z)$ reaches its saturation value c during the monotonic loading process, while the same does not occur for the 85–30 specimen as the material continues to harden beyond the maximum applied strain. For 85–15 (Figs. 12(c) and 12(d)), the saturation value is reached much before the attainment of ultimate stress, and therefore, any variation in β_c has only a slight influence on the loading response at small strains (~1%–5%). For 85–00 (Figs. 12(a) and 12(b)), the saturation value is reached near the end of the loading process, and therefore, the influence of variation in β_c on the stress–strain response is comparatively larger than 85–15. For 85–30 (Figs. 12(e) and 12(f)), however, any variation in β_c has a significant impact on the stress–strain response. It is specifically observed that β_c controls only the evolution of stress, with the stress at any strain increasing with increasing β_c and vice versa. With regard to the magnitude of β_c , a higher value of β_c increases the rate of evolution of $f(z)$ and therefore the rate of attainment of the saturation value. Hence, 85–15 has the highest value of β_c (944.2924), followed by 85–00 (125.3399), while 85–30 assumes a much lower value (2.0906).

As discussed before, the role of parameters s and β_s in the context of PBX material is to reduce the saturation value of the scale function $f(z)$ from c to c/s during the cyclic loading process in order to achieve progressive stress-softening until cyclic stabilization. While s primarily controls the magnitude of the softening, β_s controls the softening rate or the rate of attainment of cyclic stabilization. From the estimated values of s for the three specimens, the value of c/s is obtained as 11.9027, 14.4811, and 99.0748 for 85–00, 85–15, and 85–30 respectively, resulting in a reduction of 20.58%, 50.94%, and 83.24% in their respective saturation values at cyclic stabilization as compared to c . This implies that the magnitude of softening is the highest for 85–30, followed by 85–15, and the least for 85–00. Concurrently, the estimated values of β_s for the three specimens indicate the highest rate of stabilization for 85–00 (212.6798), followed by 85–15 (16.7109), and the lowest for 85–30 (5.7283). These findings with reference to the model parameters are in agreement with the experimental data, as shown in Fig. 13, where the ratio of cyclic peak stresses with respect to the first peak stress (Fig. 13(a)) drops the highest for 85–30, followed by 85–15 and then 85–00, while the change in peak stress with each cycle (Fig. 13(b)) approaches zero (i.e., cyclic stabilization) fastest for 85–00, followed by 85–15 and then 85–30.

5.3 Isotropic Damage. As shown in Secs. 2.1 and 2.3, the primary function of the isotropic damage model is to represent the overall softening between loading and unloading responses during cyclic loading of particle-binder composites. The model consists of two positive parameters m and p , each of which, according to Eq. (17), increase (decrease) the softening effect as their values decrease (increase). Figure 14 shows the influence of variation in

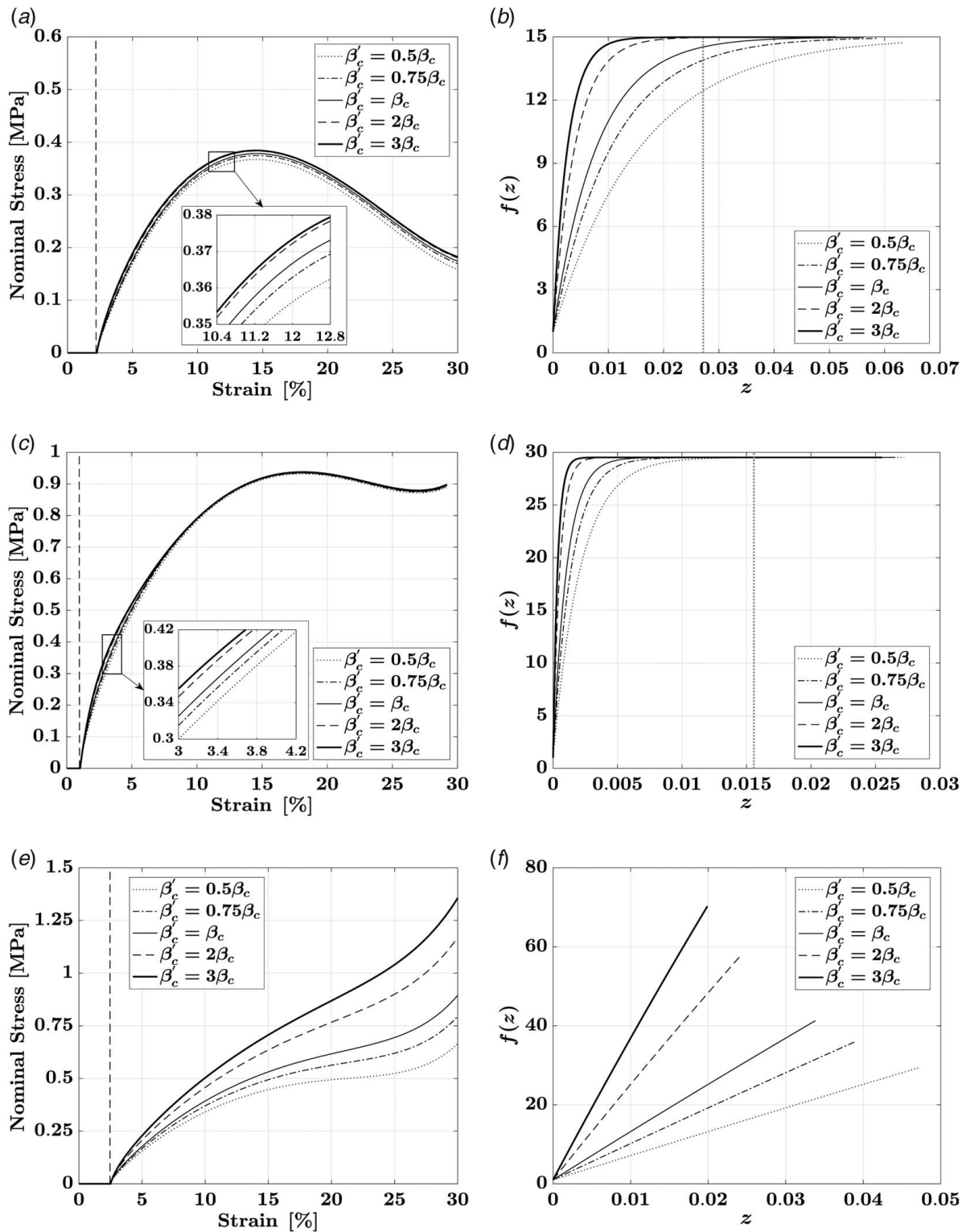


Fig. 12 (a) Influence of variation in the value of material scale function parameter β_c on the monotonic compressive response and the corresponding evolution of the material scale function $f(z)$ with intrinsic time z , for (a) and (b) 85–00; (c) and (d) 85–15; and (e) and (f) 85–30 mock formulations. The occurrence of ultimate stress in 85–00 and 85–15 is designated in their respective $f(z)$ evolution plots by a dotted line

m and p from their estimated values on a simulated load–unload response from 16% strain for the 85–15 formulation. It is observed that p predominantly affects the softening rate at higher strains, more specifically, near the beginning of unloading. On the contrary, m exerts a predominant control at lower strain levels. A closer observation of Fig. 14 indicates that the effects of p are dominant

during the initial rapid softening (~ 15 – 16% strain in the figure), while the influence of m predominates thereafter when the softening rate decreases. Figure 15 shows the evolution of the slope of the first cyclic unloading curve for the experimental cyclic compressive response of the three mock PBX specimens. The slope is plotted for the first 2% strain after the start of unloading since it is seen

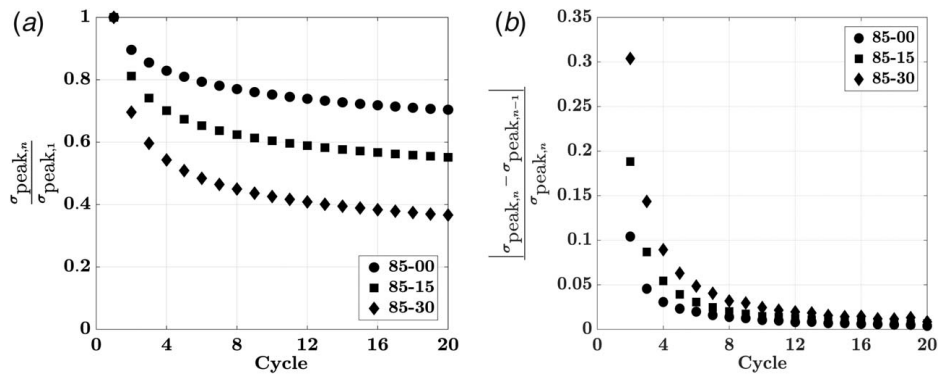


Fig. 13 (a) Plots depicting evolution of (a) the ratio of peak stress for each cycle with respect to peak stress for the first cycle, and (b) fractional change in peak stress for a cycle with respect to peak stress for the previous cycle, for cyclic compressive experimental data of 85–00, 85–15, and 85–30 specimens

that within this range the unloading curves of all three specimens begin to curve and the softening rate declines. Therefore, the effects of both m and p can be studied within this range for the three specimen compositions. From the figure, it is evident that the 85–30 specimen begins unloading with the highest slope and, therefore, exhibits the highest rate of initial softening, followed by 85–15 and then by 85–00. This is in agreement with the decreasing trend of the estimated p values in Table 1 with increasing aluminum content. With further unloading, the slope of the stress–strain curve drops rapidly for all specimens and then approaches a stable value, indicating more linear stress–strain response beyond

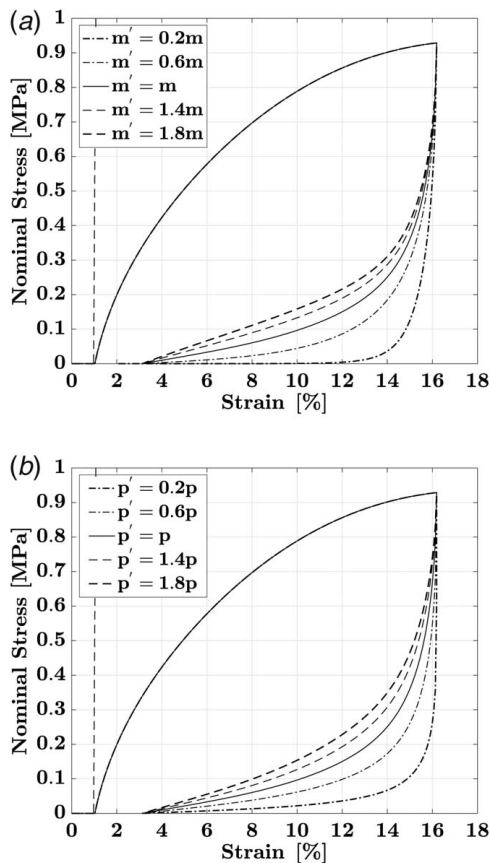


Fig. 14 (a) Influence of variation in the value of damage function parameters (a) m and (b) p on the simulated compressive load–unload response of the 85–15 formulation

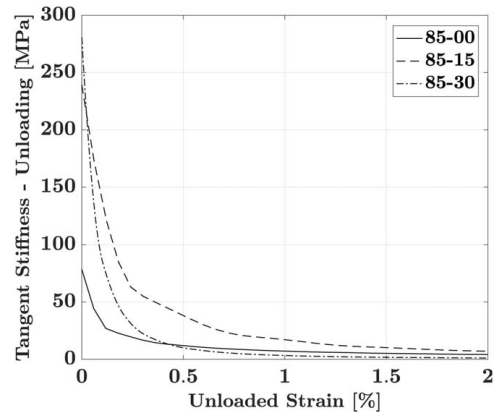


Fig. 15 Plot depicting the slope or tangent stiffness of the experimental unloading stress–strain curve during the first cycle with respect to the unloaded strain for the three mock PBX compositions

~0.5% unloaded strain. In this region, the influence of parameter m is predominant and a lower slope indicates a higher softening effect (Figure 14(a)). Therefore, 85–30 again experiences the highest softening in this strain range since it has the lowest slope. However, the slope of 85–00 is lower than 85–15 in this range and, therefore, exhibits a higher softening. This is again in agreement with the estimated values of m in Table 1, which is the highest for 85–15, followed by 85–00 and lowest for 85–30.

6 Summary and Discussion

We have presented a constitutive model for particle–binder composites that accounts for finite–deformation kinematics, nonlinear elastoplasticity without apparent yield, cyclic hysteresis, and progressive stress–softening before the attainment of stable cyclic response. The model is based on an additive decomposition of strain energy into elastic and inelastic parts, where the elastic response is modeled using Ogden hyperelasticity while the inelastic response is described using yield–surface–free endochronic plasticity based on the concepts of internal variables and of evolution or rate equations. Stress–softening is modeled using two approaches; a discontinuous isotropic damage model to appropriately describe the overall softening between loading and unloading responses, and a material scale function to describe the progressive cyclic softening until the attainment of stable response. The constitutive model is then based on the deformation mechanisms

experimentally observed during cyclic compression of PBX at large strain.

Furthermore, we have proposed a discrete numerical procedure to solve for stresses along a loading path, and we have developed a parameter identification method, based on a nonlinear multivariate minimization problem, to determine material properties from experimental nominal stress–strain data. Specifically, we have used monotonic and cyclic compression data for three mock PBX formulations based on PBXN-109 with varying aluminum content [23] to demonstrate the range of behavior predicted by the proposed constitutive model and the effectiveness of the parameter identification method. This is evident from the remarkable model calibration results that yielded an excellent agreement between experimental data and model response. Finally, we have identified the correlation between the mechanical properties and the unique stress–strain response of each specimen, which contributes toward establishing and validating specific trends observed in the property values with respect to the specimen composition, specifically, the amount of aluminum in the mock PBX. We, therefore, conclude that each of the estimated material parameters is more than a mere number and has a significant contribution toward the establishment of the highly complex and nonlinear mechanical behavior of particle-binder composites under finite strain. Based on these conclusions, the constitutive model presented in this paper serves as a reliable tool to characterize different compositions of particle-binder composites, and it especially serves the defense and propulsion communities in their efforts to characterize the mechanical properties of both existing and new energetic material formulations.

We close by pointing out some limitations of our approach and possible directions for the future extension of our analysis. First, we have restricted our attention to quasi-static, i.e., low strain-rate behavior of particle-binder composites, and thereby neglected any strain-rate-dependent effects in the constitutive model. However, it is well known that viscous effects become dominant in these materials at moderate to high strain rates. Second, the proposed constitutive model carries an assumption of elastoplastic incompressibility, which limits the analysis to particle-binder composites with moderate levels of compressibility. Therefore, the extension of the model to rate-dependent viscous effects and compressible behavior is a worthwhile direction for future research.

Acknowledgment

The authors wish to acknowledge Professor Patricia Davies, Professor Jeff Rhoads, Professor Steve Son, Professor Stuart Bolton, Jelena Paripovic, Allison Range, Nick Cummock, and Tim Manship for their feedback and interesting discussions.

Conflict of Interest

There are no conflicts of interest.

Data Availability Statement

The data sets generated and supporting the findings of this article are obtainable from the corresponding author upon reasonable request. Data provided by a third party are listed in Acknowledgment.

This research is supported by the Air Force Research Laboratory through Grant No. FA8651-16-0287 entitled “Near-Resonant Thermomechanics of Energetic and Mock Energetic Composite Materials,” Grant No. FA8651-16-D-0287 entitled “Near-Resonant Thermomechanics of Energetic and Mock Energetic Composite Materials, Part II,” and Grant No. FA8651-17-S-0003 entitled “Exploring the Thermomechanics of Energetic and Mock Energetic Composite Materials Under Quasi-Static and Near-Resonant Excitations.”

Distribution Statement

Approved for public release. Distribution unlimited (AFRL-2021-2732).

References

- [1] Rattanasom, N., Saowapark, T., and Deepseretkul, C., 2007, “Reinforcement of Natural Rubber With Silica/Carbon Black Hybrid Filler,” *Polym. Test.*, **26**(3), pp. 369–377.
- [2] Omnes, B., Thuillier, S., Pilvin, P., Grohens, Y., and Gillet, S., 2008, “Effective Properties of Carbon Black Filled Natural Rubber: Experiments and Modeling,” *Compos. Pt. A-Appl. Sci. Manuf.*, **39**(7), pp. 1141–1149.
- [3] Akhavan, J., 2011, *Chemistry of Explosives*, Royal Society of Chemistry, Cambridge, UK.
- [4] Palmer, S. J. P., Field, J. E., and Huntley, J. M., 1993, “Deformation, Strengths and Strains to Failure of Polymer Bonded Explosives,” *Proc. R. Soc. London, A*, **440**(1909), pp. 399–419.
- [5] Rae, P. J., Goldrein, H. T., Palmer, S. J. P., Field, J. E., and Lewis, A. L., 2002, Quasi-static Studies of the Deformation and Failure of β -HMX Based Polymer Bonded Explosives, *Proc. Math. Phys. Eng. Sci.*, **458**(2019), pp. 743–762.
- [6] Rangaswamy, P., Thompson, D. G., Liu, C., and Lewis, M. W., 2010, “Modeling the Mechanical Response of PBX9501,” Proceedings of the 14th International Detonation Symposium, Coeur D’Alene, ID, Apr. 11–16, pp. 174–183.
- [7] Yılmaz, G. A., Şen, D., Kaya, Z. T., and Tinger, T., 2014, “Effect of Inert Plasticizers on Mechanical, Thermal, and Sensitivity Properties of Polyurethane-Based Plastic Bonded Explosives,” *J. Appl. Polym. Sci.*, **131**(20), p. 40907.
- [8] Kumar, A., Rao, V., Sinha, R., and Rao, A., 2010, “Evaluation of Plastic Bonded Explosive (PBX) Formulations Based on RDX, Aluminum, and HTPB for Underwater Applications,” *Propellants, Explos., Pyrotech.*, **35**(4), pp. 359–364.
- [9] Wiegand, D. A., 2000, “The Influence of Confinement on the Mechanical Properties of Energetic Materials,” *AIP Conf. Proc.*, **505**(1), pp. 675–678.
- [10] Wiegand, D. A., and Reddingius, B., 2005, “Mechanical Properties of Confined Explosives,” *J. Energ. Mater.*, **23**(2), pp. 75–98.
- [11] Drodge, D. R., and Williamson, D. M., 2016, “Understanding Damage in Polymer-Bonded Explosive Composites,” *J. Mater. Sci.*, **51**(2), pp. 668–679.
- [12] Idar, D. J., Thompson, D. G., Gray, G. T., Blumenthal, W. R., Cady, C. M., Peterson, P. D., Roemer, E. L., Wright, W. J., and Jacquez, B. J., 2002, “Influence of Polymer Molecular Weight, Temperature, and Strain Rate on the Mechanical Properties of PBX 9501,” *AIP Conf. Proc.*, **620**(1), pp. 821–824.
- [13] Thompson, D. G., Idar, D. J., Gray, G., Blumenthal, W. R., Cady, C. M., Roemer, E. L., Wright, W. J., and Peterson, P. D., 2002, “Quasi-static and Dynamic Mechanical Properties of New and Virtually-Aged PBX 9501 Composites as a Function of Temperature and Strain Rate,” Proceedings of the 12th International Detonation Symposium, San Diego, CA, Aug. 11–16, pp. 363–368.
- [14] Williamson, D. M., Siviour, C. R., Proud, W. G., Palmer, S. J. P., Govier, R., Ellis, K., Blackwell, P., and Leppard, C., 2008, “Temperature-Time Response of a Polymer Bonded Explosive in Compression (EDC37),” *J. Phys. D: Appl. Phys.*, **41**(8), p. 085404.
- [15] Bardenhagen, S., Harstad, E., Maudlin, P., Gray, G., and Foster Jr, J., 1998, “Viscoelastic Models for Explosive Binder Materials,” *AIP Conf. Proc.*, **429**(1), pp. 281–284.
- [16] Clements, B. E., and Mas, E. M., 2001, “Dynamic Mechanical Behavior of Filled Polymers. I. Theoretical Developments,” *J. Appl. Phys.*, **90**(11), pp. 5522–5534.
- [17] Bennett, J. G., Haberman, K. S., Johnson, J. N., and Asay, B. W., 1998, “A Constitutive Model for the Non-shock Ignition and Mechanical Response of High Explosives,” *J. Mech. Phys. Solids*, **46**(12), pp. 2303–2322.
- [18] Addressio, F. L., and Johnson, J. N., 1990, “A Constitutive Model for the Dynamic Response of Brittle Materials,” *J. Appl. Phys.*, **67**(7), pp. 3275–3286.
- [19] Dienes, J. K., 1996, “A Unified Theory of Flow, Hot Spots, and Fragmentation With an Application to Explosive Sensitivity,” *High-Pressure Shock Compression of Solids II: Dynamic Fracture and Fragmentation*, L. Davison, D. E. Grady, and M. Shahinpoor, eds., Springer, New York, pp. 366–398.
- [20] Buechler, M. A., and Luscher, D. J., 2014, “A Semi-implicit Integration Scheme for a Combined Viscoelastic-Damage Model of Plastic Bonded Explosives,” *Int. J. Numer. Methods Eng.*, **99**(1), pp. 54–78.
- [21] Paripovic, J., and Davies, P., 2013, “Identification of the Dynamic Behavior of Surrogate Explosive Materials,” International Design Engineering Technical Conferences and Computers and Information in Engineering Conference; 22nd Reliability, Stress Analysis, and Failure Prevention Conference; 25th Conference on Mechanical Vibration and Noise, Portland, OR, Aug. 4–7, ASME, p. V008T13A066.
- [22] Paripovic, J., and Davies, P., 2016, “A Model Identification Technique to Characterize the Low Frequency Behaviour of Surrogate Explosive Materials,” *J. Phys. Conf. Ser.*, **744**, p. 012124.
- [23] Agarwal, A., and Gonzalez, M., 2020, “Effects of Cyclic Loading and Time-Recovery on Microstructure and Mechanical Properties of Particle-Binder Composites,” *ASME J. Appl. Mech.*, **87**(10), p. 101008.
- [24] Lochert, I. J., Dexter, R. M., and Hamshere, B. L., 2002, *Evaluation of Australian RDX in PBXN-109, DSTO-TN-0440*, Defence Science, Technology Organisation, Weapons Systems Division, Edinburgh (SA), Australia.

- [25] Pijaudier-Cabot, G., Bittnar, Z., and Gérard, B., 1999, *Mechanics of Quasi-brittle Materials and Structures*, Hermes Science Publications, Paris, France.
- [26] Idar, D., Peterson, P., Scott, P., and Funk, D., 1998, "Low Strain Rate Compression Measurements of PBXN-9, PBX9501, and Mock 9501," *AIP Conf. Proc.*, **429**(1), pp. 587–590.
- [27] Trumel, H., Lambert, P., and Biessy, M., 2012, "Mechanical and Microstructural Characterization of a HMX-Based Pressed Explosive: Effects of Combined High Pressure and Strain Rate," *EPJ Web Conf.*, **26**, p. 02005.
- [28] Keyhani, A., Kim, S., Horie, Y., and Zhou, M., 2019, "Energy Dissipation in Polymer-Bonded Explosives With Various Levels of Constituent Plasticity and Internal Friction," *Comput. Mater. Sci.*, **159**, pp. 136–149.
- [29] Le, V. D., Gratton, M., Caliez, M., Frachon, A., and Picart, D., 2010, "Experimental Mechanical Characterization of Plastic-Bonded Explosives," *J. Mater. Sci.*, **45**(21), pp. 5802–5813.
- [30] Yang, K., Wu, Y., and Huang, F., 2018, "Numerical Simulations of Microcrack-Related Damage and Ignition Behavior of Mild-Impacted Polymer Bonded Explosives," *J. Hazard. Mater.*, **356**, pp. 34–52.
- [31] Tang, M., Pang, H., Lan, L., Wen, M., and Ming, L., 2016, "Constitutive Behavior of RDX-Based PBX With Loading-History and Loading-Rate Effects," *Chin. J. Energ. Mater.*, **24**(9), pp. 832–837.
- [32] Laiarinandrasana, L., Piques, R., and Robisson, A., 2003, "Visco-hyperelastic Model With Internal State Variable Coupled With Discontinuous Damage Concept Under Total Lagrangian Formulation," *Int. J. Plast.*, **19**(7), pp. 977–1000.
- [33] Ayoub, G., Zaïri, F., Naït-Abdelaziz, M., Gloaguen, J. M., and Kridli, G., 2014, "A Visco-hyperelastic Damage Model for Cyclic Stress-Softening, Hysteresis and Permanent Set in Rubber Using the Network Alteration Theory," *Int. J. Plast.*, **54**, pp. 19–33.
- [34] Österlöf, R., Wentzel, H., and Kari, L., 2016, "A Finite Strain Viscoplastic Constitutive Model for Rubber With Reinforcing Fillers," *Int. J. Plast.*, **87**, pp. 1–14.
- [35] Guo, Q., Zaïri, F., and Guo, X., 2018, "A Thermo-viscoelastic-Damage Constitutive Model for Cyclically Loaded Rubbers. Part I: Model Formulation and Numerical Examples," *Int. J. Plast.*, **101**, pp. 106–124.
- [36] Guo, Q., Zaïri, F., and Guo, X., 2018, "A Thermo-Viscoelastic-Damage Constitutive Model for Cyclically Loaded Rubbers. Part II: Experimental Studies and Parameter Identification," *Int. J. Plast.*, **101**, pp. 58–73.
- [37] Chen, Y., Kang, G., Yuan, J., and Yu, C., 2018, "Uniaxial Ratcheting of Filled Rubber: Experiments and Damage-Coupled Hyper-viscoelastic-Plastic Constitutive Model," *ASME J. Appl. Mech.*, **85**(6), p. 061013.
- [38] Dargazany, R., Khiêm, V. N., and Itskov, M., 2014, "A Generalized Network Decomposition Model for the Quasi-static Inelastic Behavior of Filled Elastomers," *Int. J. Plast.*, **63**, pp. 94–109.
- [39] Raghunath, R., Juhre, D., and Klüppel, M., 2016, "A Physically Motivated Model for Filled Elastomers Including Strain Rate and Amplitude Dependency in Finite Viscoelasticity," *Int. J. Plast.*, **78**, pp. 223–241.
- [40] Plagge, J., and Klüppel, M., 2017, "A Physically Based Model of Stress Softening and Hysteresis of Filled Rubber Including Rate- and Temperature Dependency," *Int. J. Plast.*, **89**, pp. 173–196.
- [41] Mullins, L., 1948, "Effect of Stretching on the Properties of Rubber," *Rubber Chem. Technol.*, **21**(2), pp. 281–300.
- [42] Mullins, L., 1969, "Softening of Rubber by Deformation," *Rubber Chem. Technol.*, **42**(1), pp. 339–362.
- [43] Marckmann, G., Verron, E., Gornet, L., Chagnon, G., Charrier, P., and Fort, P., 2002, "A Theory of Network Alteration for the Mullins Effect," *J. Mech. Phys. Solids*, **50**(9), pp. 2011–2028.
- [44] Chagnon, G., Verron, E., Marckmann, G., and Gornet, L., 2006, "Development of New Constitutive Equations for the Mullins Effect in Rubber Using the Network Alteration Theory," *Int. J. Solids Struct.*, **43**(22), pp. 6817–6831.
- [45] Klüppel, M., 2003, "The Role of Disorder in Filler Reinforcement of Elastomers on Various Length Scales," *Filler-Reinforced Elastomers Scanning Force Microscopy*, 1, Vol. 164, B. Capella, M. Geuss, M. Klüppel, M. Munz, E. Schulz, and H. Sturm, eds., Springer, Berlin/Heidelberg, pp. 1–86.
- [46] Kaliske, M., and Rothert, H., 1998, "Constitutive Approach to Rate-Independent Properties of Filled Elastomers," *Int. J. Solids Struct.*, **35**(17), pp. 2057–2071.
- [47] Valanis, K. C., 1970, *A Theory of Viscoplasticity Without a Yield Surface Part I—General Theory*, Air Force Office of Scientific Research, Office of Aerospace Research, US Air Force, Arlington, VA.
- [48] Netzker, C., Dal, H., and Kaliske, M., 2010, "An Endochronic Plasticity Formulation for Filled Rubber," *Int. J. Solids Struct.*, **47**(18–19), pp. 2371–2379.
- [49] Simo, J. C., 1987, "On a Fully Three-Dimensional Finite-Strain Viscoelastic Damage Model: Formulation and Computational Aspects," *Comput. Methods Appl. Mech. Eng.*, **60**(2), pp. 153–173.
- [50] Govindjee, S., and Simo, J., 1991, "A Micro-mechanically Based Continuum Damage Model for Carbon Black-Filled Rubbers Incorporating Mullins' Effect," *J. Mech. Phys. Solids*, **39**(1), pp. 87–112.
- [51] Holzapfel, G. A., and Simo, J. C., 1996, "A New Viscoelastic Constitutive Model for Continuous Media at Finite Thermomechanical Changes," *Int. J. Solids Struct.*, **33**(20), pp. 3019–3034.
- [52] Holzapfel, G. A., 1996, "On Large Strain Viscoelasticity: Continuum Formulation and Finite Element Applications to Elastomeric Structures," *Int. J. Numer. Methods Eng.*, **39**(22), pp. 3903–3926.
- [53] Holzapfel, G. A., 2002, "Nonlinear Solid Mechanics: A Continuum Approach for Engineering Science," *Meccanica*, **37**(4), pp. 489–490.
- [54] Ogden, R. W., 1972, "Large Deformation Isotropic Elasticity on the Correlation of Theory and Experiment for Incompressible Rubberlike Solids," *Proc. R. Soc. London, Ser. A*, **326**(1567), pp. 565–584.
- [55] Ogden, R. W., 1972, "Large Deformation Isotropic Elasticity: On the Correlation of Theory and Experiment for Compressible Rubberlike Solids," *Proc. R. Soc. London, Ser. A*, **328**(1575), pp. 567–583.
- [56] Horstemeyer, M. F., and Bammann, D. J., 2010, "Historical Review of Internal State Variable Theory for Inelasticity," *Int. J. Plast.*, **26**(9), pp. 1310–1334.
- [57] Kachanov, L. M., 1986, *Introduction to Continuum Damage Mechanics*, Springer, Netherlands.
- [58] Lemaitre, J., Chaboche, J.-L., and Germain, P., 1985, *Mécanique Des Matériaux Solides*, Dunod, Paris, France.
- [59] Wu, H., and Yip, M., 1981, "Endochronic Description of Cyclic Hardening Behavior for Metallic Materials," *ASME J. Eng. Mater. Technol.*, **103**(3), pp. 212–217.
- [60] Yeh, W.-C., 1995, "Verification of the Endochronic Theory of Plasticity Under Biaxial Load," *J. Chin. Inst. Eng.*, **18**(1), pp. 25–34.
- [61] Lin, H.-Y., Yeh, W.-C., and Lee, W.-J., 2007, "A Material Function of Endochronic Theory and Its Application to Test Under Axisymmetrically Cyclic Loading Conditions," *J. Mech.*, **23**(2), pp. 135–148.
- [62] Kröner, E., 1959, "Allgemeine Kontinuumstheorie Der Versetzungen Und Eigenspannungen," *Arch. Ration. Mech. Anal.*, **4**(1), pp. 273–334.
- [63] Lee, E., and Liu, D., 1967, "Finite-Strain Elastic-Plastic Theory With Application to Plane-Wave Analysis," *J. Appl. Phys.*, **38**(1), pp. 19–27.
- [64] Lee, E. H., 1969, "Elastic-Plastic Deformation at Finite Strains," *ASME J. Appl. Mech.*, **36**(1), pp. 1–6.
- [65] Gurtin, M. E., and Anand, L., 2005, "The Decomposition $F = F^e F^p$, Material Symmetry, and Plastic Irrotationality for Solids That Are Isotropic-Viscoplastic or Amorphous," *Int. J. Plast.*, **21**(9), pp. 1686–1719.
- [66] Hill, R., 1950, *The Mathematical Theory of Plasticity*, Clarendon Press, Oxford, UK.
- [67] Hill, R., 1958, "A General Theory of Uniqueness and Stability in Elastic-Plastic Solids," *J. Mech. Phys. Solids*, **6**(3), pp. 236–249.
- [68] Prager, W., 1961, "An Elementary Discussion of Definitions of Stress Rate," *Q. Appl. Math.*, **18**(4), pp. 403–407.
- [69] Blanchard, A. F., and Parkinson, D., 1952, "Breakage of Carbon-Rubber Networks by Applied Stress," *Ind. Eng. Chem.*, **44**(4), pp. 799–812.
- [70] Bueche, F., 1960, "Molecular Basis for the Mullins Effect," *J. Appl. Polym. Sci.*, **4**(10), pp. 107–114.
- [71] Houwink, R., 1956, "Slipping of Molecules During the Deformation of Reinforced Rubber," *Rubber Chem. Technol.*, **29**(3), pp. 888–893.
- [72] Clément, F., Bokobza, L., and Monnerie, L., 2001, "On the Mullins Effect in Silica-Filled Polydimethylsiloxane Networks," *Rubber Chem. Technol.*, **74**(5), pp. 847–870.
- [73] Kraus, G., Childers, C. W., and Rollmann, K. W., 1966, "Stress Softening in Carbon Black-Reinforced Vulcanizates. Strain Rate and Temperature Effects," *J. Appl. Polym. Sci.*, **10**(2), pp. 229–244.
- [74] Klüppel, M., and Schramm, J., 2000, "A Generalized Tube Model of Rubber Elasticity and Stress Softening of Filler Reinforced Elastomer Systems," *Macromol. Theory Simul.*, **9**(9), pp. 742–754.
- [75] Ogden, R. W., and Roxburgh, D. G., 1999, "A Pseudoelastic Model for the Mullins Effect in Filled Rubber," *Proc. R. Soc. London, Ser. A*, **455**(1988), pp. 2861–2877.
- [76] Dorfmann, A., and Ogden, R. W., 2003, "A Pseudo-elastic Model for Loading, Partial Unloading and Reloading of Particle-Reinforced Rubber," *Int. J. Solids Struct.*, **40**(11), pp. 2699–2714.
- [77] Zúñiga, A. E., and Beatty, M. F., 2002, "A New Phenomenological Model for Stress-Softening in Elastomers," *J. Appl. Math. Phys.*, **53**(5), pp. 794–814.
- [78] Miehe, C., 1995, "Discontinuous and Continuous Damage Evolution in Ogden-Type Large-Strain Elastic Materials," *Eur. J. Mech. A Solids*, **14**(5), pp. 697–720.
- [79] Kaliske, M., Nasdala, L., and Rothert, H., 2001, "On Damage Modelling for Elastic and Viscoelastic Materials at Large Strain," *Comput. Struct.*, **79**(22–25), pp. 2133–2141.
- [80] Lin, R. C., and Schomburg, U., 2003, "A Finite Elastic-Viscoelastic-Elastoplastic Material Law With Damage: Theoretical and Numerical Aspects," *Comput. Methods Appl. Mech. Eng.*, **192**(13–14), pp. 1591–1627.
- [81] Rickaby, S. R., and Scott, N. H., 2013, "Cyclic Stress-Softening Model for the Mullins Effect in Compression," *Int. J. Non Linear Mech.*, **49**, pp. 152–158.
- [82] Diani, J., Fayolle, B., and Gilormini, P., 2009, "A Review on the Mullins Effect," *Eur. Polym. J.*, **45**(3), pp. 601–612.
- [83] Naumann, C., and Ihlemann, J., 2015, "On the Thermodynamics of Pseudo-elastic Material Models Which Reproduce the Mullins Effect," *Int. J. Solids Struct.*, **69–70**, pp. 360–369.
- [84] Coleman, B. D., and Noll, W., 1963, "The Thermodynamics of Elastic Materials With Heat Conduction and Viscosity," *Arch. Ration. Mech. Anal.*, **13**(1), pp. 167–178.
- [85] Coleman, B. D., and Gurtin, M. E., 1967, "Thermodynamics With Internal State Variables," *J. Chem. Phys.*, **47**(2), pp. 597–613.
- [86] Mooney, M., 1940, "A Theory of Large Elastic Deformation," *J. Appl. Phys.*, **11**(9), pp. 582–592.
- [87] Rivlin, R., 1948, "Large Elastic Deformations of Isotropic Materials IV. Further Developments of the General Theory," *Philos. Trans. Royal Soc.*, **241**(835), pp. 379–397.
- [88] Boyce, M. C., and Arruda, E. M., 2000, "Constitutive Models of Rubber Elasticity: A Review," *Rubber Chem. Technol.*, **73**(3), pp. 504–523.

- [89] Ogden, R. W., 1984, *Non-linear Elastic Deformations*, Dover Publications, Mineola, NY.
- [90] Beatty, M. F., and Krishnaswamy, S., 2000, "A Theory of Stress-Softening in Incompressible Isotropic Materials," *J. Mech. Phys. Solids*, **48**(9), pp. 1931–1965.
- [91] Valanis, K. C., and Lee, C., 1984, "Endochronic Theory of Cyclic Plasticity With Applications," *ASME J. Appl. Mech.*, **51**(2), pp. 367–374.
- [92] Guo, J., Wu, L., Yang, X., and Zhong, S., 2016, "Elastic-Plastic Endochronic Constitutive Model of 0Cr17Ni4Cu4Nb Stainless Steels," *Math. Probl. Eng.*, **2016**, pp. 1–16.
- [93] Valanis, K., and Read, H., 1986, "An Endochronic Plasticity Theory for Concrete," *Mech. Mater.*, **5**(3), pp. 277–295.
- [94] Bakhshiani, A., Khoei, A., and Mofid, M., 2002, "An Endochronic Plasticity Model for Powder Compaction Processes," *J. Mater. Process. Technol.*, **125–126**, pp. 138–143.
- [95] Khoei, A., Bakhshiani, A., and Mofid, M., 2003, "An Endochronic Plasticity Model for Finite Strain Deformation of Powder Forming Processes," *Finite Elem. Anal. Des.*, **40**(2), pp. 187–211.
- [96] Khoei, A., and Bakhshiani, A., 2004, "A Hypoelasto-Plastic Finite Strain Simulation of Powder Compaction Processes With Density-Dependent Endochronic Model," *Int. J. Solids Struct.*, **41**(22–23), pp. 6081–6110.
- [97] Hsu, S. Y., Jain, S. K., and Griffin, O. H., 1991, "Verification of Endochronic Theory for Nonproportional Loading Paths," *J. Eng. Mech.*, **117**(1), pp. 110–131.
- [98] Valanis, K. C., 1972, *Irreversible Thermodynamics of Continuous Media: Internal Variable Theory*, Vol. 1, Springer, Vienna.
- [99] Coleman, B. D., 1964, "Thermodynamics of Materials With Memory," *Arch. Ration. Mech. Anal.*, **17**(1), pp. 1–46.
- [100] MATLAB®, Version 9.4.0.2018, Natick, Massachusetts: The Mathworks Inc., 1984–2018.